
Louisiana Transportation Research Center

Final Report 14-2TIRE

**Hurricane Hazard Mitigation in Traffic Light
Support Structures**

by

Aly Mousaad Aly, Ph.D., Hamzeh Gol Zaroudi,
and Milad Rezaee

LSU



4101 Gourrier Avenue | Baton Rouge, Louisiana 70808
(225) 767-9131 | (225) 767-9108 fax | www.ltrc.lsu.edu

TECHNICAL REPORT STANDARD PAGE

1. Report No. FHWA/LA.15/14-2TIRE		2. Government Accession No.		3. Recipient's Catalog No.			
4. Title and Subtitle Hurricane Hazard Mitigation in Traffic Light Support Structures		5. Report Date January 2016		6. Performing Organization Code LTRC Project Number: 14-2TIRE State Project Number: DOTDLT1000032			
		7. Author(s) Aly Mousaad Aly, Ph.D., Hamzeh Gol Zaroudi, and Milad Rezaee				8. Performing Organization Report No.	
9. Performing Organization Name and Address Department of Civil and Environmental Engineering Louisiana State University Baton Rouge, LA 70803		10. Work Unit No.				11. Contract or Grant No.	
		12. Sponsoring Agency Name and Address Louisiana Department of Transportation and Development P.O. Box 94245 Baton Rouge, LA 70804-9245		13. Type of Report and Period Covered Final Report July 2014 - June 2015		14. Sponsoring Agency Code	
15. Supplementary Notes Conducted in Cooperation with the U.S. Department of Transportation, Federal Highway Administration							
16. Abstract Traffic signs and signals are extensively used as vital elements in highways and urban roads for communicating with drivers, in order to convey the rules, guidance, warnings, and other highway agency information. On this basis, it is crucial to have reliable and well-maintained traffic signs and signals to ascertain that essential messages are properly conveyed to drivers in various environmental conditions. Long mast arm cantilever structures are widely used on highways all over the world. Cantilevered traffic signal support structures are slender, lightly-damped structures, and since they may have a span as long as 66 ft, they are very flexible structures, and highly sensitive to wind-induced vibrations, and their fatigue life is an important issue in the design process. Another important concern about traffic signal structures is their vulnerability in critical weather conditions, such as during hurricanes. The serviceability of these structures during hurricanes is extremely important due to their critical role in directing traffic, specifically for evacuation and rescue operation. Consequently, this study presents a methodology to suppress wind-induced vibrations in a mast arm cantilever traffic signal with a circular cylinder section, by using computational fluid dynamics (CFD) simulations to create wind load time series and a dynamic model for structural control. For wind load simulations, a time-dependent approach by implementing the Large Eddy Simulation (LES) was used. Monitoring points are defined on the mast arm to capture pressure coefficients, and then calculate distributed lift and drag forces at different sections. The simulated time histories of drag and lift forces are then used for the control purpose, after experimental validation. In order to mitigate the vibrations, distributed tuned mass dampers are investigated, making use of the available weights of the lighting boxes. The structural response with and without the dampers are simulated by a dynamic model. The dynamic analysis shows that damping enhancement in traffic lighting structures can significantly reduce vibration-induced stress, with promises to improve the safety to the traveling public, extend the life of existing traffic structures, increase traffic efficiency, and reduce the cost of new structures. Moreover, the generated wind load time histories with the dynamic model are being used for different vibration control schemes, including passive and semi-active control devices with drift magnification connections, with the objective of building a database useful for creating guidelines and recommendations on the proper use of damping enhancement devices, for future implementation in the AASHTO standard.							
17. Key Words traffic signal support structures; wind load estimation; pressure coefficients; Large Eddy Simulation (LES); tuned mass damper; vibration mitigation.			18. Distribution Statement Unrestricted. This document is available through the National Technical Information Service, Springfield, VA 21161.				
19. Security Classif. (of this report) N/A		20. Security Classif. (of this page) N/A		21. No. of Pages 107			
				22. Price N/A			

Project Review Committee

Each research project will have an advisory committee appointed by the LTRC Director. The Project Review Committee is responsible for assisting the LTRC Administrator or Manager in the development of acceptable research problem statements, requests for proposals, review of research proposals, oversight of approved research projects, and implementation of findings.

LTRC appreciates the dedication of the following Project Review Committee Members in guiding this research study to fruition.

LTRC Manager

Walid R. Alaywan, Ph.D., P.E.
Sr. Structures Research Engineer

Directorate Implementation Sponsor

Janice P. Williams, P.E.
DOTD Chief Engineer

Hurricane Hazard Mitigation in Traffic Light Support Structures

by

Aly Mousaad Aly, Ph.D.
Assistant Professor

Hamzeh Gol Zaroudi
Graduate Student

Milad Rezaee
Graduate Student

Department of Civil and Environmental Engineering
3513D Patrick F. Taylor Hall
Louisiana State University
Baton Rouge, LA 70803

LTRC Project No. 14-2TIRE
State Project No. DOTDLT1000032

conducted for

Louisiana Department of Transportation and Development
Louisiana Transportation Research Center

The contents of this report reflect the views of the author/principal investigator who is responsible for the facts and the accuracy of the data presented herein. The contents do not necessarily reflect the views or policies of the Louisiana Department of Transportation and Development or the Louisiana Transportation Research Center. This report does not constitute a standard, specification, or regulation.

January 2016

ABSTRACT

Traffic signs and signals are extensively used as vital elements in highways and urban roads for communicating with drivers, in order to convey the rules, guidance, warnings, and other highway agency information. On this basis, it is crucial to have reliable and well-maintained traffic signs and signals to ascertain that essential messages are properly conveyed to the drivers in various environmental conditions. Long mast arm cantilever structures are widely used on the highways all over the world. Cantilevered traffic signal support structures are slender, lightly damped structures, and since they may have a span as long as 66 feet, they are very flexible structures and highly sensitive to wind-induced vibrations, and their fatigue life is an important issue in the design process. Another important concern about traffic signal structures is their vulnerability in critical weather conditions, such as during hurricanes. The serviceability of these structures during hurricanes is extremely important due to their critical role in directing traffic, specifically for evacuation and rescue operation. Consequently, this study presents a methodology to suppress wind-induced vibrations in a mast arm cantilever traffic signal with a circular cylinder section, by using computational fluid dynamics (CFD) simulations to create wind load time series and a dynamic model for structural control. For wind load simulations, a time-dependent approach by implementing the Large Eddy Simulation (LES) was used. Monitoring points are defined on the mast arm to capture pressure coefficients, and then calculate distributed lift and drag forces at different sections. The simulated time histories of drag and lift forces are then used for the control purpose, after experimental validation. In order to mitigate the vibrations, distributed tuned mass dampers are investigated, making use of the available weights of the lighting boxes. The structural response with and without the dampers are simulated by a dynamic model. The dynamic analysis shows that damping enhancement in traffic lighting structures can significantly reduce vibration-induced stress, with promises to improve the safety to the traveling public, extend the life of existing traffic structures, increase traffic efficiency, and reduce the cost of new structures. Moreover, the generated wind load time histories with the dynamic model are being used for different vibration control schemes, including passive and semi-active control devices with drift magnification connections, with the objective of building a database useful for creating guidelines and recommendations on the proper use of damping enhancement devices, for future implementation in the AASHTO standard.

ACKNOWLEDGMENTS

The PI would like to acknowledge the funding support for this research by the Louisiana Department of Transportation and Development (DOTD) through the Louisiana Transportation Research Center (LTRC). Thanks to Dr. Walid Alaywan for his support of this research. The High Performance Computing (HPC) facilities at LSU were used in the current study, such computer allocation from LSU is acknowledged. The PI would like to acknowledge the travel grant provided by NSF through the American Association for Wind Engineering (AAWE), to attend the 14th International Conference on Wind Engineering (ICWE14), and to present the results of this study in a technical proceeding paper with an oral presentation. Thanks to LTRC for agreeing to publish the results of this report.

IMPLEMENTATION STATEMENT

The results obtained from the current project show promises to using Computational Fluid Dynamic simulations to obtain wind loads on traffic support structures at full-scale. With such wind loading data, a dynamic model of the primary structure with any type of damping enhancement devices (when properly modeled) can be used to investigate its performance, a crucial step towards the standardization of the use of damping enhancement techniques. The methodology presented in this report is applicable to investigate the performance of damping devices, for potential implementation in the AASHTO design standard.

TABLE OF CONTENTS

ABSTRACT.....	iii
ACKNOWLEDGMENTS	v
IMPLEMENTATION STATEMENT	vii
TABLE OF CONTENTS.....	ix
LIST OF TABLES.....	xi
LIST OF FIGURES	xiii
INTRODUCTION	1
Wind Excitation Forces.....	2
Vortex Shedding	2
Galloping.....	4
Natural Wind Gusts.....	5
Truck-Induced Wind Gusts.....	5
Summary of Wind Excitation Forces.....	6
Types of Wind-Induced Failures in Traffic Lighting Support Structures.....	6
Fatigue-Related Failures	6
Hurricane-Caused Failures.....	15
Connections-Related failures	16
Fatigue Design	17
Simplification of Dynamic Fatigue Loads.....	17
Fatigue Importance Factors.....	18
Fatigue Design Loads	18
Literature on Vibration Suppression.....	20
OBJECTIVE	29
SCOPE	31
METHODOLOGY	33
Modelling of Hurricane Loading on a Traffic Lighting Support Structure	34
2-D Numerical CFD Model	37
Experimental Study of the Model.....	43
Comparison between CFD and Experiment Results.....	50
3-D CFD Simulation of the Model	54
Boundary Conditions and Meshing Procedure	55
Turbulence Model Used for the Simulation.....	55
Input Wind Velocity Profile.....	58
Drag and Lift Calculations.....	59
3-D Wind Model Results	60

Transient Inflow Wind Spectrum and Turbulence Intensity.....	61
Dimensionless Pressure Coefficients (Cp).....	63
Final Simulated Drag and Lift Forces.....	64
Vibration Mitigation	66
Equation of Motion for the Multi-Degree Freedom System.....	67
Generation of the Mass, Stiffness and Damping Matrices	68
Tuned Mass Damper	69
Dynamic Study.....	71
DISCUSSION OF RESULTS.....	75
CONCLUSIONS.....	77
RECOMMENDATIONS.....	79
ACRONYMS, ABBREVIATIONS, AND SYMBOLS	81
REFERENCES	83

LIST OF TABLES

Table 1 Summary of in- and out-of-plane results for various dampers used by Hamilton et al.	22
Table 2 Summary of various types of damping devices investigated by Cook et al.	23
Table 3 Damper types studied for vibration mitigation of traffic signal structures.....	25
Table 4 Various cases for mesh independence study.....	38
Table 5 Diameter, wind speed, and Reynolds number for each experimental cases.....	45
Table 6 The results of experimental tests	49

LIST OF FIGURES

Figure 1 Failure in traffic lighting support structures.....	2
Figure 2 The formation of vortex shedding.	3
Figure 3 Variation of Strouhal number with Reynolds number.	4
Figure 4 Fatigue failure of a mast arm in Lubbock, Texas.....	7
Figure 5 Location of sign supports S-61-0001 and S-61-0002 in Osseo, Wisconsin.....	8
Figure 6 Photograph of fracture surface for sign S-61-0001.....	9
Figure 7 Dye penetrant analysis results for S-61-001 from Osseo, Wisconsin.....	9
Figure 8 Dye penetrant analysis results for S-61-002 from Osseo, Wisconsin.....	10
Figure 9 View of signal support structure in Wyoming that has partially collapsed.....	11
Figure 10 Typical box-type detail for the mast-arm-to-post connection for traffic signal supports.....	12
Figure 11 Cracks forming at the top of the stiffeners.....	13
Figure 12 Weld toe failure of a full penetration connection (left) and external collar failure (right).....	13
Figure 13 Mast arm fatigue failure.....	14
Figure 14 Failure of traffic signal support structure in Tampa, FL. 2013.....	14
Figure 15 Wind-induced fatigue damage and collapses.....	15
Figure 16 Signal support structure failure by the Hurricane Katrina, New Orleans, LA.....	16
Figure 17 Lakeview area, New Orleans, LA. Aftermath of Hurricane Katrina.....	16
Figure 18 Improperly fabricated detail for welded attachment of shelf plate to post.....	17
Figure 19 Strut and shock absorber damper.....	21
Figure 20 In-plain strut.....	26
Figure 21 Smart damper (SHVA) developed by Christenson.....	27
Figure 22 Typical single mast arm and pole assembly.....	33
Figure 23 Field test of 60-ft. mast arm with vertically mounted signal heads.....	36
Figure 24 2-D domain for CDF analysis and structured mesh with finer mesh sizes.....	37
Figure 25 Distribution of mean pressure coefficient around the cylinder for 4 CFD RSM cases.....	39
Figure 26 Lift coefficient history for the RSM 2-D with 468 K cells and flow velocity of 14.47 mph.....	40
Figure 27 Drag coefficient for the RSM 2-D with 468 K cells and flow velocity of 14.47 mph.....	41
Figure 28 Power Spectrum Density for Drag and Lift coefficients for the RSM 2-D case.....	42
Figure 29 Distribution of mean pressure coefficient around the cylinder for	

4 CFD RSM cases.	43
Figure 30 LSU’s wind tunnel: (a) boundary-layer test section; (b) flow conditioner.	44
Figure 31 Open-jet simulations: (a) main concept (b) small-scale open-jet simulator at LSU.....	44
Figure 32 Schematic representation of the circular cylinder geometry and the domain.	45
Figure 33 The experimental set up and connecting the pressure measurements sensors	46
Figure 34 Experimental setup for the first model with $D = 4.5$ in.....	46
Figure 35 Experimental setup for the second model with $D = 6.63$ in.	47
Figure 36 Experimental setup.	48
Figure 37 Distribution of mean pressure coefficient around the cylinder for 3 experimental cases.	49
Figure 38 Distribution of mean pressure coefficient around the cylinder for 2 experimental cases.....	50
Figure 39 Distribution of mean pressure coefficient around the cylinder for 2 cases.	51
Figure 40 Distribution of mean pressure coefficient around the cylinder for 2 cases.	52
Figure 41 Distribution of mean pressure coefficient around the cylinder for 2 cases.	53
Figure 42 Spectra of the wind velocities upstream and downstream.....	53
Figure 43 The methodology used for the 3-D aerodynamic analysis of traffic support structure	54
Figure 44 Mesh generated computational domain.....	55
Figure 45 Simulated inlet wind speed profile.....	59
Figure 46 Points defined on the arm surface to measure the pressure coefficient.....	60
Figure 47 Time history of wind velocity in X- direction at reference height.	62
Figure 48 Results of input wind velocity profile.	62
Figure 49 Mean value of time series of area-weighted averaged pressure coefficient within the monitoring points	63
Figure 50 Distribution of mean pressure coefficient around the cylinder for 2 cases.	64
Figure 51 Lift with standard deviation of $\text{std} = 32.38$ [N], and drag with $\text{std} = 16.99$ [N]	65
Figure 52 Time series of wind-induced loads on the different parts of the mast arm	66
Figure 53 Methodology were used for the dynamic study	67
Figure 54 Concentrated masses through the mast arm	68
Figure 55 Changing the frequency and damping ratios of the TMD.....	71
Figure 56 Equivalent system damping ratio for different mass ratios.....	71
Figure 57 Cantilevered signal support structure used for simulation	72
Figure 58 Modal shapes of the cantilevered support structure.....	72
Figure 59 Modal shapes of the cantilevered support structure.....	73
Figure 60 Displacement of the mast arm free-end for controlled and	

uncontrolled structure.....	73
Figure 61 Stress at the mast arm fixed-end for controlled and uncontrolled structure.....	73

INTRODUCTION

Traffic signs and signals are extensively used as vital elements in highways and urban roads for communicating with drivers in order to convey the rules, guidance, warnings, and other highway agency information. On this basis, it is crucial to have reliable and well-maintained traffic signs and signals in order to make certain that the desired messages are properly conveyed to the drivers on the streets in various environmental conditions. Among the support structures, long mast arm cantilever structures are widely used on highways all over the world, and especially in the United States. Cantilevered traffic signal support structures are considered as slender, lightly damped structures and since they may have a span as long as 66 ft., they are very flexible structures, and highly sensitive to the wind-induced vibrations, and their fatigue life is an important issue in the design process [1]. An important concern about traffic signal support structures is their vulnerability in critical weather conditions such as in hurricanes. The serviceability of these structures during hurricanes is extremely important due to their critical role in directing traffic, specifically for evacuation and rescue operation during an event. These concerns highlight the importance of vibration mitigation in flexible cantilever traffic lighting support structures.

Cruzado indicates that the flexibility of these structures results in a low fundamental natural frequency at which the signal structure will resonate with large amplitudes of vibration [2]. According to Cook et al., natural frequencies observed in mast arm structures are typically in the range of 0.7 Hz to 1.4 Hz [3]. Long span mast arms with traffic signals can resonate visibly at any wind speed. Kaczinski et al. mentioned that mast arm displacements are reported in excess of 4 ft. under steady state winds with speeds in the range of 10 to 35 mph [4]. Such large displacements under wind loads are responsible of fatigue failure in the traffic light support structures.

Fatigue failure is the most common type of failure in cantilevered mast arms. Missouri had over 12 traffic signal mast arms failure in a period of six years [5]. Similar failures were reported in Wyoming, California, and Texas [6]. Figure 1(a) shows one of the two fatigue failures that occurred from 2001 to 2005 in Lubbock, Texas [7, 8]. Figure 1(b) also shows wind-induced cracks forming at the top of the stiffeners when the post to baseplate connection is reinforced with stiffeners [4].

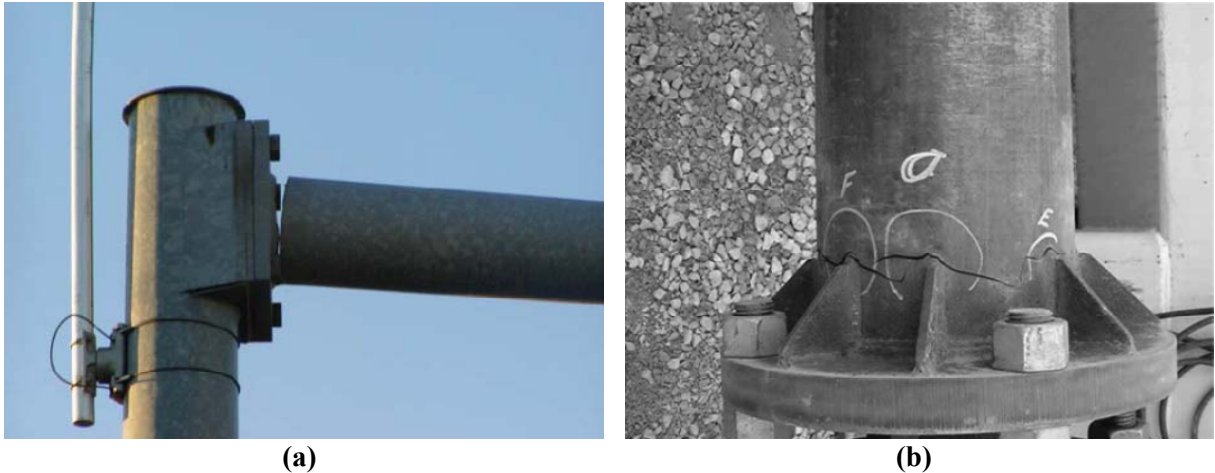


Figure 1
Failure in traffic lighting support structures

Considering their inherent flexibility, complex wind loading scenarios like vortex shedding and/or galloping effects can cause fatigue failure of these structures, even under low to moderate wind speeds, in the order of 10 to 30 mph [9]. In addition, wind loads due to tornadoes, hurricanes, or other extreme winds can cause the failure. Recently in April 2015, tornadoes tore through parts of Iowa, Illinois, and Ohio, which was first forecasted and warned by the National Weather Service as a “particularly dangerous situation.” It caused massive damages, including some homes with only their foundations remaining [10]. Considering these serious hazards in the US, it is essential to conduct research studies on the investigation of wind and storm-induced loads on the transportation infrastructure. In parallel with damping enhancement and vibration mitigation in traffic lightening support structures, the purpose of this study is to present a methodology to obtain wind loads at real Reynolds numbers using CFD with LES, with experimental validation by aerodynamic tests at the newly -built, open-jet facility at Louisiana State University (LSU).

Wind Excitation Forces

Christenson classified various types of wind loading that can result in traffic signal support vibration as: vortex shedding, natural wind gusts, truck-induced gusts, and galloping [11].

Vortex Shedding

As airflow travels over a bluff body, it reaches points of separation on each side where thin sheets of tiny vortices are generated. As the vortex sheets detach, they interact with one another and roll up into discrete vortices that are shed alternately from the sides of the object. Figure 2 shows vortex shedding around a circular cylinder obtained by CFD simulations carried out in the current study. The asymmetric pressure distribution created by the vortices

around the cross section results in a sinusoidal forcing function transverse to the air flow's direction (in the case of horizontal mast arms, this results in vertical motion). When the vortex shedding frequency approaches the natural frequency of a structure, it results in an increase in vortex strength and a tendency for the vortex shedding frequency to couple with the frequency of the structure [12].

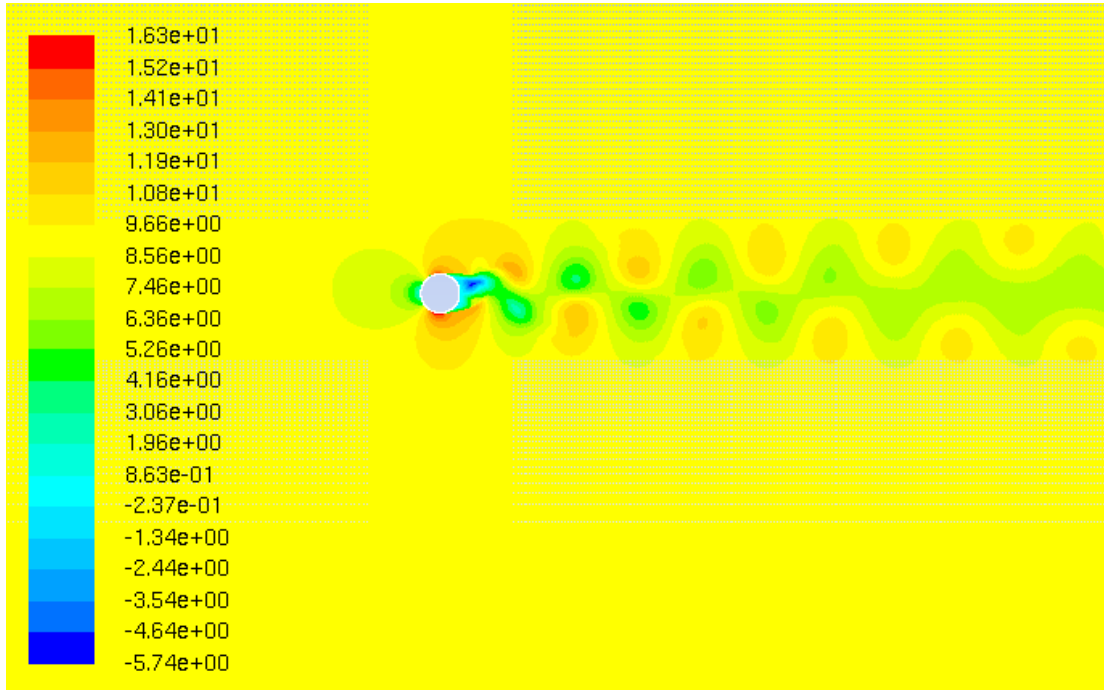


Figure 2
The formation of vortex shedding

The frequency of shedding vortices can be calculated using the Strouhal relation:

$$f_s = \frac{S \cdot V}{D} \quad (1)$$

where, S is the Strouhal number, D is the across-wind dimension of the element, and V is the freestream wind velocity [4]. Since uniform steady-state flow is required for vortex shedding, velocity boundaries can be determined for a mast arm susceptibility to vortex-induced oscillations [13]. Figure 3 shows the relation between the Strouhal number and Reynolds number (which is defined by flow velocity), and defining various regions in which the vortex shedding can happen [14].

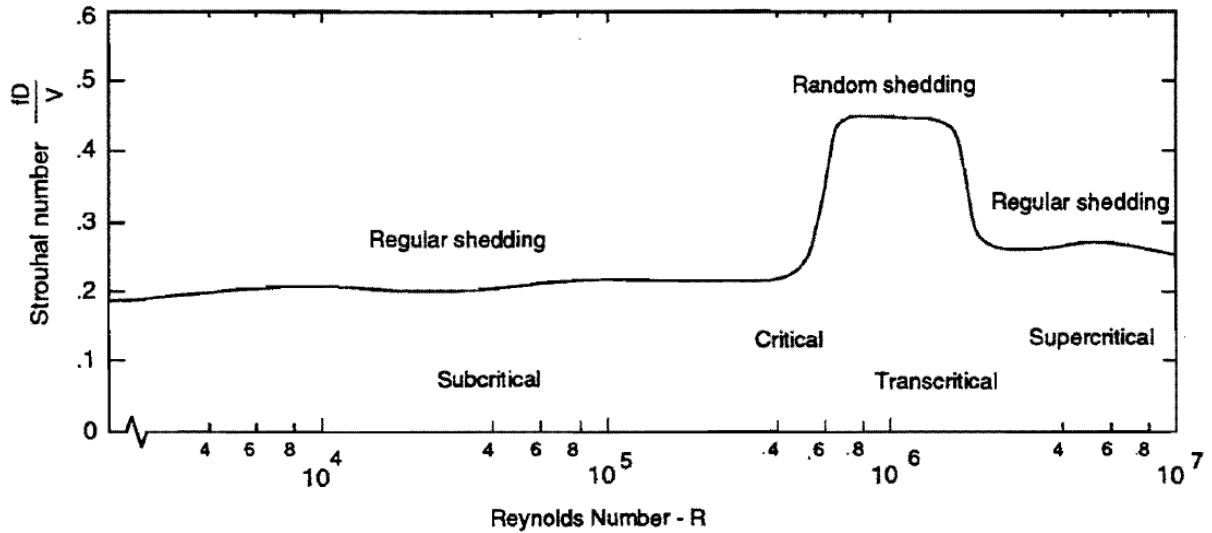


Figure 3
Variation of Strouhal number with Reynolds number

Previous research indicates that the level of turbulence associated with wind velocities above approximately 35 to 40 mph limits the symmetric formation of periodic vortices [15]. Also, vortex formation at wind velocities below approximately 10 mph generates forces with magnitudes insufficient to excite most structures. Therefore, structures may be susceptible to vortex-induced oscillations in the range of wind velocities between approximately 10 to 35 mph. The vortex shedding phenomenon does not appear to have a significant effect on cantilevered mast arm structures with diameter less than 3 ft. Nevertheless, Zuo & Letchford showed that vortex-shedding cause large-amplitude vibrations in the structure at low wind speeds while at high speed winds, the structure vibrates due to buffeting at amplitudes smaller than those of the vortex-induced vibrations [16]. These findings differ from previous observations where large-amplitude vibrations of this type of traffic-signal-support structures were attributed to galloping caused by the interaction between the traffic signals and/or the back plates and the wind [16]. In any case, due to the height of most vertically mounted traffic signals, it is possible that vortex shedding could play a role in initiating of the galloping phenomenon [13].

Galloping

Galloping is an unstable phenomenon caused by aerodynamic forces generated on certain cross-sectional shapes resulting in displacements transverse to the wind [17]. For horizontal structures subjected to wind, the resulting motion occurs in the vertical plane. For a circular section located in a steady air stream of velocity, V , if the body moves upward at a velocity, u , a resultant wind force will act on it at a downward angle of attack, α , given by [13]:

	$\alpha = \arctan\left(\frac{U}{V}\right)$	(2)
--	--	-----

This resultant wind force will cause a drag force and a lift force on the section. It should be noted that galloping cannot start when the structure is at rest. Wind gusts usually start structural movement and then oscillations continue [18]. Galloping oscillations may have a significant effect on cantilevered traffic signal structures. As noted by Kaczinski et al. and McDonald et al. Kaczinski et al., galloping is most likely the primary cause of excessive vibrations in these types of structures [9] and [4]. Hamilton et al. hypothesize that due to the overall interaction of the entire mast arm structure, galloping may also initiate horizontal motion [19].

Natural Wind Gusts

Natural wind gusts arise from the variability in velocity (speed and direction) of airflow. These wind gusts are characterized by a spectrum of velocity components that oscillate over a broad range of frequencies as a result of turbulence inherently present in any natural airflow [4]. This broad range of frequencies causes the amplitude and direction of a structure's response to be variable and randomly distributed. The pressure imposed to the structure due to the gust can be estimated by a ratio called gust factor, which is defined as the ratio of the expected peak displacement load during a specified period to the mean displacement load. According to the AASHTO, this factor for design of sign, signal, and luminaire support structures is 1.3 [13]. Kaczinski et al. reported that all evidence indicates that cantilevered support structures perform satisfactorily under extreme gust loading conditions. Hence, the factor recommended by AASHTO is adequate for the ultimate strength design of mast arm support structures [4].

Truck-Induced Wind Gusts

Truck-induced wind gusts on cantilevered mast arm structures are the result of large vehicles repeatedly passing beneath the structures. Creamer et al. performed research in this area on trussed sign structures with natural frequencies in the range of 1.5 to 2.0 Hz and found that the generated wind pressures were quite small [20]. For example, peak pressure due to a truck traveling beneath the traffic signal structure is equal to the peak pressure due to the wind with more than 2.8 times less in speed. Also in this research, it was found that the frequency of the truck-induced wind gusts is directly proportional to the length of the truck and the speed at which it traveled. Moreover, it was shown that the frequency range of wind gusts and the mast arm structure are very close and therefore, although the resulting pressures are small, the likelihood of matching of frequencies between the loading and the structures

can induce excessive vibrations [12]. In another study conducted by Cook et al. at the University of Florida, the wind pressure given off by semi-trucks along a major highway was studied [21]. It was determined that the trucks produced wind gusts at frequencies around 2 Hz and 0.5 Hz and, since these frequencies are close to the natural frequencies of long mast arms located along high-speed roads, therefore, truck induced-gusts also can be responsible for oscillations for these structures.

Summary of Wind Excitation Forces

Based on the literature, different phenomena can be responsible for mast arm vibrations including vortex shedding, galloping, natural wind gusts, and truck-induced wind gusts. However, various studies show that wind-induced galloping is the primary cause of excessive vibrations in traffic signal support structures and vortex shedding is probably the least likely cause of oscillations due to the tapered geometry of most horizontal cantileveres [4, 13, and 22]. Nevertheless, Zuo & Letchford showed that vortex-shedding causes large-amplitude vibrations in the structure at low wind speeds, while at high speed winds, the structure vibrates due to buffeting at amplitudes smaller than those of the vortex-induced vibrations [16]. These findings differ from previous observations where large-amplitude vibrations of this type of traffic-signal-support structures were attributed to galloping caused by the interaction between the traffic signals and/or the back plates and the wind [16]. According to literature, natural wind gusts effects are not very significant and truck-induced wind gusts can cause relatively small and quick vibrations.

Types of Wind-Induced Failures in Traffic Lighting Support Structures

Fatigue Related Failures

Failure due to fatigue is the most common type of failure for cantilevered mast arms. Missouri had over 12 traffic signal mast arms fail in a period of six years [5]. Similar failures were reported in Wyoming, California, and Texas [6]. Figure 4 shows one of two fatigue failures that occurred from 2001 to 2005 in Lubbock, Texas [7] and [8].



Figure 4
Fatigue failure of a mast Arm in Lubbock, Texas

There is a fundamental expression that relates the magnitude of a stress range cycle (stress-ranges) to the number of times that stress-range cycle can be applied before crack initiation in a metal [23]:

$$N.(S_R)^m = A \quad (3)$$

where, N is the fatigue life of the detail and corresponds to the number of stress-range cycles accumulated at failure or initial crack formation; S_R is the constant stress-range cycle magnitude applied; A is the fatigue detail constant; and m is an exponent describing the slope of the SR-N curve for the specific detail category.

In fall 2011, two sign support structures, S-61-0001 and S-61-0002, in Osseo, Wisconsin, were reported to have circumferential cracks at the weld toes of the tube-to-plate connections of their mast-arms [23]. Figure 5 shows a view of the location of these two traffic sign structures [23]. The signs were located on the northbound and southbound exit ramps from U.S. Interstate Highway 94 to U.S. Highway 10. The supports of the signs were found to be

cracked in October 2011. According to Foley et al., this failure was driven by fatigue [23]. It should be noted that the support structures went into service in 2003 and were designed in a time frame where provisions for considering fatigue were included in design specifications [24]. Figure 6, Figure 7, and Figure 8 preview the cracks in these two sign structures [25]. Dye penetrant evaluation defined the extent of the cracking in these photos.

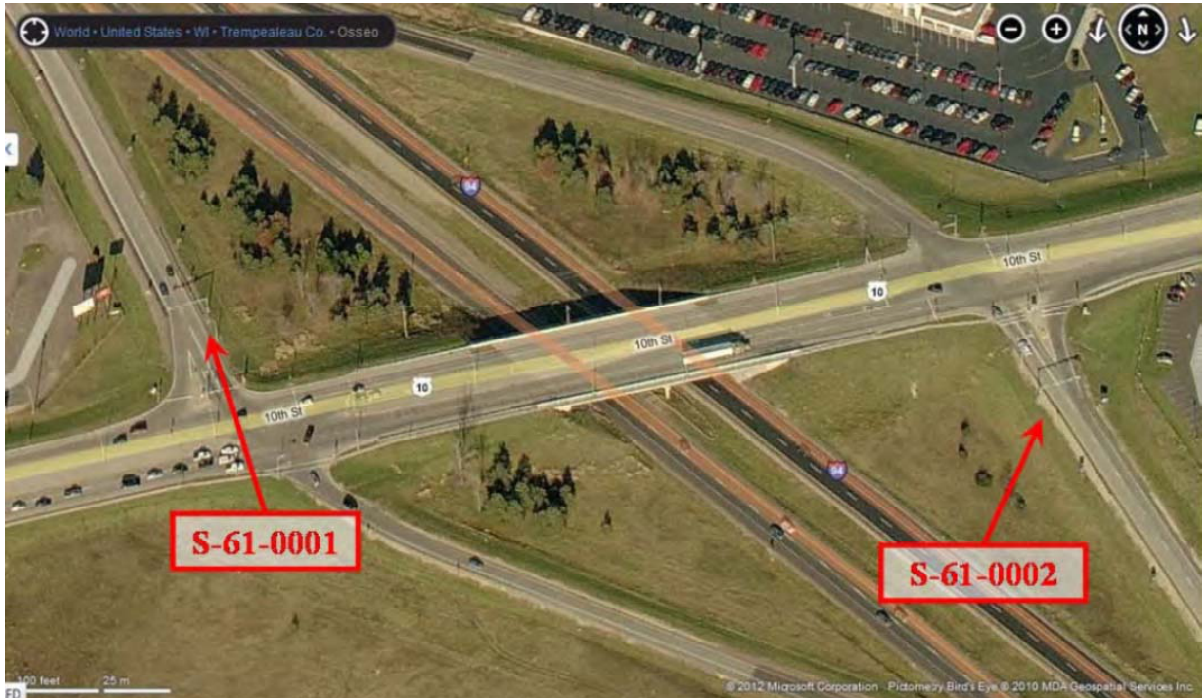


Figure 5
Location of sign supports S-61-0001 and S-61-0002 in Osseo, Wisconsin

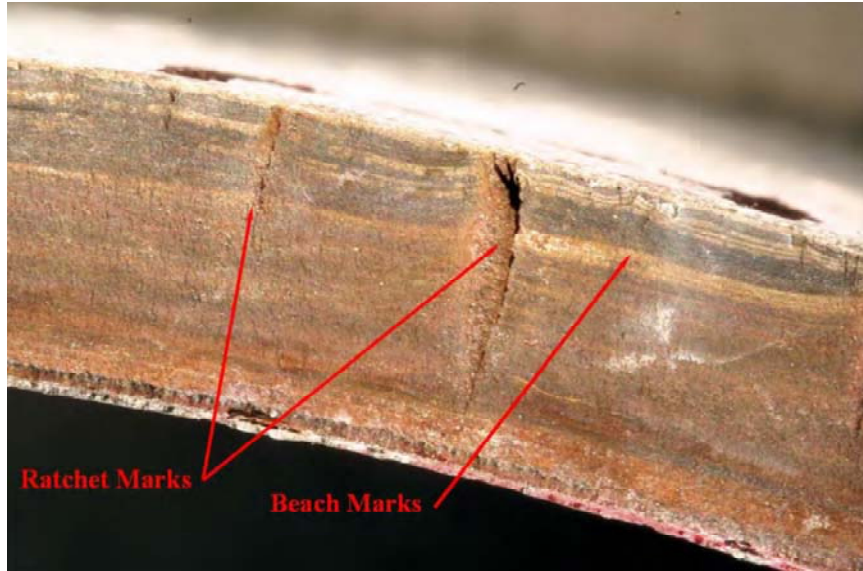


Figure 6
Photograph of Fracture Surface for Sign S-61-0001



Figure 7
Dye penetrant analysis results for S-61-001 from Osseo, Wisconsin



Figure 8
Dye penetrant analysis results for S-61-002 from Osseo, Wisconsin

The wind-induced motion at the tip of the mast arm of a cantilevered sign or signal support structure may distract drivers if the range exceeds 7.87 in [4]. Moreover, it can cause fatigue cracks and collapse in these cantilevered support structures even at the motion ranges that cannot be noticed without sensors. Figure 9 shows a signal support structure in Wyoming where the mast arm has collapsed due to fatigue cracking of the mast arm to pole connection [4]. Inadequate design specifications prior to 2001 may be one of the main reasons of failures in these structures fabricated before 2001, when the 4th edition of the *Standard Specifications for Structural Supports for Highway Signs, Luminaires and Traffic Signals* was introduced. Explicit fatigue design criteria including fatigue loads and a catalog of the fatigue strength of various details are addressed in this edition.



Figure 9
View of signal support structure in Wyoming that has partially collapsed

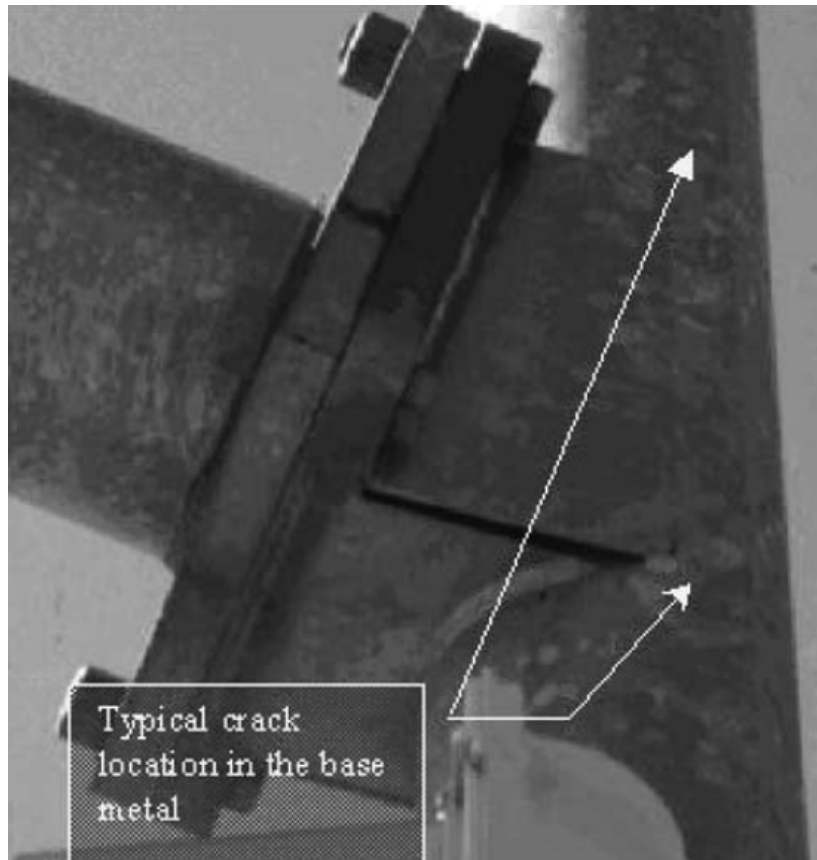


Figure 10

Typical box-type detail for the mast-arm-to-post connection for traffic signal supports

Connections of built-up box (mast arm connection) to the post, which is typically used in cantilevered signal support structures, has caused fatigue cracking in many states, including Wyoming. Typical locations of the cracks along the toe of the weld between the sides of the box and the post are shown in Figure 10 [26]. This type of cracking is believed to be caused by stress ranges in the side plates of the box [4].

The other vulnerable point that cracks may occur is at the base of the poles where the cracks may form at the weld joining the pole to the baseplate. Here, if there are stiffeners or gussets reinforcing the pole to baseplate connection, then the cracks will typically form at the tops of the stiffeners. Figure 11 shows cracks that formed at the top of stiffeners in a fatigue test, when the post to baseplate connection is reinforced with stiffeners. In this case, the stiffeners are too short and not sufficiently tapered to be fully effective [4].



Figure 11
Cracks forming at the top of the stiffeners

Richman investigated two typical fatigue failures, including full penetration and external collar of mast arm base plate connections, as shown in Figure 12 [27]. The results for round and octagonal poles compared and concluded that (1) there is no practical difference in the fatigue performance of full penetration details with round or octagonal poles; (2) the shape of the base plate and orientation of bolt holes in full penetration details has a slight effect on the fatigue performance on the connection as a relatively minor factor; (3) round full penetration details, octagonal full penetration details, and external collars exhibit similar fatigue performance and all perform much better than a socket connection but octagonal external collars may not perform as well as round external collars; and (4) thicker base plates improve the fatigue performance of full penetration connections [27].



Figure 12
Weld toe failure of a full penetration connection (left) and external collar failure (right)

Figure 13 and Figure 14 depict a typical service fatigue failure that occurs when the crack at the toe of the fillet weld connecting the end plate to the arm [28, 29]. Another example is shown in Figure 15 [30]. The figure shows a 98.5-ft. pole that collapsed due to wind-induced fatigue.



Figure 13
Mast arm fatigue failure



Figure 14
Failure of traffic signal support structure in Tampa, FL, 2013



Figure 15
Wind-induced fatigue damage and collapses

Hurricane-Caused Failures

Hurricanes are responsible for part of failure events in transportation infrastructures including traffic signal support structures. Figure 16 and Figure 17 show traffic mast arm structures that collapsed during Hurricane Katrina in New Orleans, LA. [31] and [32]. The failure happened due to the strong effect of the hurricane on the structure.



Figure 16
Signal support structure failure by the Hurricane Katrina, New Orleans, LA



Figure 17
Lakeview area, New Orleans, LA. Aftermath of Hurricane Katrina

Connections-Related Failures

A portion of failures that occur for mast arm structures are due to the inappropriate connections. For instance, Figure 18 shows a detail that was fabricated differently from the drawings. The drawings called for a radius cut in the shelf plate so it fit around and could be continuously welded to the post. Hence, the detail in Figure 18 would be expected to have

drastically reduced fatigue life relative to the detail shown in the drawings. Here, the contact area is very small, increasing the stress ranges significantly on the small welds from the cyclic loads. Furthermore, the small angle formed at the terminations of the fillet welds forms a notch. Notches are generally bad for fatigue [1].



Figure 18
Improperly fabricated detail for welded attachment of shelf plate to post

Fatigue Design

According to AASHTO, overhead cantilevered sign and traffic signal structures should be designed for fatigue due to individual loadings from galloping, natural wind gusts, and truck-induced wind gusts. It also indicated that vortex shedding should be considered for single-member cantilevered members that have tapers less than 0.14 in/ft, such as lighting structures or mast arms without attachments [24]. Some of the highlights are addressed as follows:

Simplification of Dynamic Fatigue Loads

Dynamic fatigue loads produced by vortex shedding, galloping, natural wind gusts, and truck induced wind gusts are simplified by using equivalent static loads, which create similar stress responses. Therefore, there is no need to conduct complex dynamic analyses in place of simple static analyses.

Fatigue Importance Factors

A fatigue importance factor (IF) accounts for the degree of hazard to traffic and damage to property. These factors are used to adjust the magnitude of the fatigue pressures. Fatigue IF's are given in AASHTO 2001 Specifications. The three important categories (Category I, Category II, and Category III) refer to (I) critical cantilevered support structures installed on major highways, (II) other cantilevered support structures installed on secondary highways, and (III) cantilevered support structures installed at all other locations, respectively. For Category I, the IFs are always 1.0. That is, the fatigue loads are not reduced. This is because Category I structures are designed to withstand the least-frequently occurring wind-induced fatigue loads and also because in the case of failure, such structures would create a greater hazard. The range of factors in Category II is from 0.65 for galloping in sign and traffic signals supports and vortex shedding in lighting poles to 0.89 for truck-induced gusts of sign supports. Category III factors are consistent with the 1994 Specifications in which fatigue provisions were not included. Factors in Category III range from 0.30 for galloping in traffic signals and vortex shedding in lighting poles to 0.77 for truck-induced gusts in sign supports. It is important to note that factors in Category II are simply the average values between values in Categories I and III [33].

Fatigue Design Loads

AASHTO 2001 Specifications indicate: "To avoid large-amplitude vibrations and to preclude the development of fatigue cracks in various connection details and at other critical locations, cantilevered support structures shall be designed to resist each of the following applicable limit state equivalent wind loads acting separately." The limit state equivalent wind loads that this statement refers to are: galloping, vortex shedding, natural wind gusts, and truck-induced wind gusts [33].

Galloping. The equivalent static load for galloping is given in terms of vertical shear pressure, which is applied on the vertical plane of mast arm attachments, such as signs, signal heads, and signal head back plates. The magnitude of the pressure developed from galloping is in terms of importance factor, IF, and is defined as:

$$PG = 21 \text{ IF (in psf)} \tag{4}$$

According to the 2001 Specifications, galloping loads may be ignored if an approved mitigation device is used. Installing a sign blank, mounted horizontally and directly above the traffic signal attachment closest to the tip of the mast arm, is an effective mitigating device for traffic signal support structures with horizontally mounted traffic signal attachments. For vertically mounted traffic signal attachments, a sign blank horizontally

mounted near the tip of the mast arm was proven to mitigate galloping vibration in traffic signals [9]. The sign blanks measured 16 in. x 66 in. Stock bridge devices were proven to work in mitigating galloping. Smaller damping plates did not effectively mitigate oscillations from galloping. Also, damping plates mounted at locations other than directly above the outermost signal attachment were not effective in mitigating this type of vibration [33].

Vortex Shedding. The equivalent static pressure range, PVS, to be applied in the direction perpendicular to the wind and to the area projected on the vertical plane, is calculated by:

$$P_{VS} = \frac{0.00118V_C^2 C_D I_F}{2\beta} \quad \text{in } psf \quad (5)$$

where, the critical wind velocity for a prismatic member, V_C , is given by:

$$V_C = \frac{f_n d}{S_n} \quad \text{for circular sections} \quad (6)$$

And

$$V_C = \frac{f_n b}{S_n} \quad \text{for multisided sections} \quad (7)$$

where,

- f_n = the first natural frequency of the structure (Hz)
- d = element diameter (m)
- b = the flat-to-flat width of the member (m)
- S_n = the Strouhal number
- C_D = the drag coefficient for the section of interest
- I_F = fatigue importance factor
- β = damping ratio (0.005)

According to the 2001 Specifications, vortex-shedding loads may be ignored if an approved mitigation device is used. In regards to vortex shedding mitigating devices, there is significant uncertainty as to what works and what does not. Further testing is needed in this area. It is important to note that, according to the 2001 AASHTO, support structures that are composed of tapered members do not appear to be prone to vortex-shedding induced vibrations when tapered at least 0.14 in/ft. However, since there are reports of tapered poles that have exhibited vortex shedding, this issue needs further research [33].

Natural Wind Gusts. Natural wind gusts are applied in the direction parallel to the wind flow to the horizontally projected areas of all members, and sign, signals, and traffic lights [33]. The pressure from natural wind gusts is calculated from:

$$P_{NW} = 5.2C_D I_F \quad (\text{in psf}) \text{ for mean speeds below 11.2 mph} \quad (8)$$

or

$$P_{NW} = 5.2C_D \left(\frac{V_m^2}{125} \right) I_F \quad (\text{in psf}) \text{ for locations with more detailed} \quad (9)$$

meteorological data

where,

$$V_m = \text{yearly mean wind velocity (mph)}$$

Truck-Induced Gusts. Truck induced gust equivalent static pressures are applied to the areas on the undersides of members, signs, signals, and other attachments. At a minimum, these pressures should be applied to the outer 12 ft. of the mast arm. This distance is equivalent to the width of one traffic lane. The truck-gust pressures, PTG, are defined as follows:

$$P_{TG} = 18.8C_D I_F \quad (\text{in psf}) \text{ for truck speeds of 65 mph} \quad (10)$$

or

$$P_{TG} = 18.8C_D \left(\frac{V}{65} \right)^2 I_F \quad (\text{in psf}) \text{ for truck speeds less than 65 mph} \quad (11)$$

where,

$$V = \text{truck velocity (mph)}$$

Literature on Vibration Suppression

In order to increase the fatigue life, the vibration of the structure under the excited loads should be reduced to a safe standard range. Different studies are undertaken in order to quantify, control, and suppress these vibrations. McDonald et al. tested a tuned mass damper, a liquid tuned damper, and a damping plate for traffic sign structures [9]. They mentioned that the problem of tuned mass dampers is their distraction of motorists. For a liquid tuned

damper, a 3-ft. piece of PVC was inserted in the end of the arm and partially filled with water. It was concluded that this mitigation method was not effective. The vibration mitigation method that they recommended was a damping plate (wing). The wing was a horizontal plate with dimensions of 16-in. by 66-in. mounted with at least 3-in. separation between the damping plate and the top of the signal light backing plate. This device was recommended because it was not a distraction to motorists, required no maintenance, and posed no problems in finding available material [12].

Cook et al. conducted an experimental study on a 37-ft. mast arm. They concluded that the traditional tuned mass damper and friction damper were more successful to reduce the vibration [3]. In a similar study, Hamilton et al. applied various types of vibration absorbers to mitigate a 50-ft. mast arm [19]. Investigation was done over elastomeric pads installed at the arm-pole and/or base connection, a strut and shock absorber installed between the pole and the mast arm (Figure 19), an Alcoa dumbbell damper, and various types of impact dampers. Their research depicted that the structure with no damper had in-plane damping of 0.15% and a fundamental period of 1.17 s. Also it had out-of-plan damping of 0.47% and a fundamental period of 1.20 s. Moreover, the findings showed that the strut and shock absorber worked very well in plane. It was noted that when the shock absorber was tested at the highest setting, the tip acceleration of the mast arm decreased up to 90%. Nevertheless, there was no increase in damping out-of-plane due to the addition of the strut and shock absorber because during out of plane movement the shock absorber remains inactive, since there is no significant relative translation between the attachment points in that case. Table 1 summarizes the results for different dampers that used in the Hamilton et al. study [19].

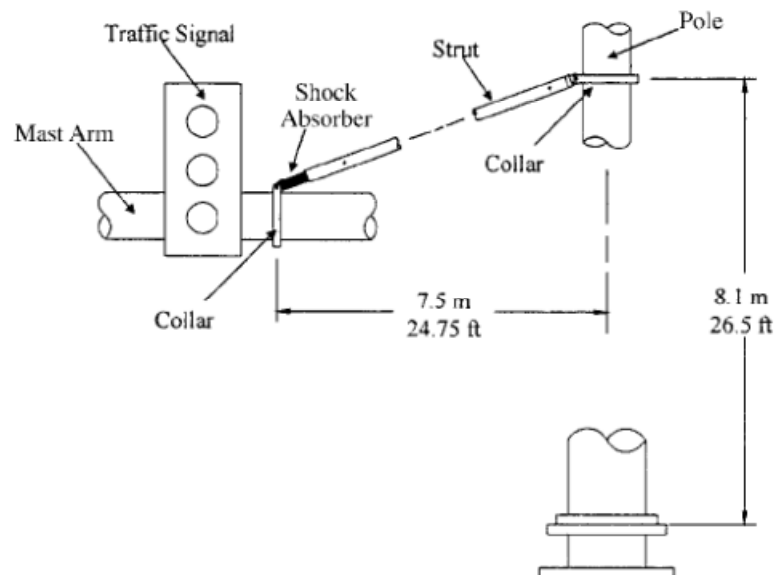


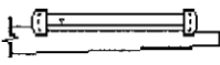
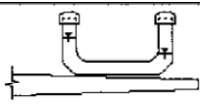
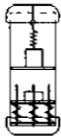
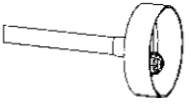
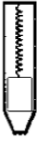
Figure 19
Strut and shock absorber damper

Table 1
Summary of in- and out-of-plane results for various dampers used by Hamilton et al.

Damping Device	In-plane Results			Out-of-plane Results		
	Damping Ratio (%)	Period (s)	Increase	Damping Ratio (%)	Period (s)	Increase
None	0.15	1.17	1.0	0.47	1.2	1.0
Pad at mast arm	0.28	1.19	1.9	0.77	1.2	1.6
Pad at mast arm and base	0.43	1.21	2.9	2.4	1.4	5.1
Pad at base	0.39	1.19	2.6	2.8	1.3	6.0
Strut	2.4-6.0	1.15	16-40	0.37-0.45	1.2	0.8-1.0
Flat bar (unconfined)	1.1	1.21	7.3			
Flat bar (1.0 s period)	0.3-1.1	1.22	2.0-7.3			
Flat bar (1.2 s period)	0.25-0.91	1.22	1.7-6.1			
Flat bar (1.4 s period)	0.30-0.37	1.22	2.0-2.5			
Hapco	0.31	1.19	2.1	0.83	1.2	1.8
Strand (1.0 s period)	0.54-1.30	1.22	3.6-8.7	1.8	1.2	3.8
Strand (1.2 s period)	0.72-1.60	1.22	4.8-10.7	1.5	1.3	3.2
Strand (1.4 s period)	0.97-1.40	1.22	6.5-9.3	1.2	1.3	2.6
Dumbbell	0.26	1.20	1.7	0.79	1.2	1.7
Shot-put	0.20-0.29	1.32	1.3-1.9	0.63-1.60	1.4	1.3-3.4
Shot-put 45 degree	0.20-0.28	1.33	1.3-1.9	0.6-1.1	1.4	1.3-2.3

Cook et al. conducted a study to develop a damping device to attenuate wind-induced vibrations in cantilevered traffic signal structures [12]. In this study, the performance of tuned mass dampers, liquid dampers, friction dampers, damping devices installed at the arm-pole connection, and impact dampers including spring/mass impact dampers, spring/mass liquid impact dampers and tapered impact dampers were investigated (Table 2). Cook et al. did not recommend tuned mass dampers due to the need to modify the damper characteristics for each installation [12]. Liquid dampers and damping devices at the arm-pole connection were not proposed for field use due to their poor performance on the laboratory mast arm. Also friction dampers rejected due to their overall height. The spring/mass impact dampers also were not recommended because of either high fabrication costs or poor performance. Hence, they selected spring/mass liquid impact dampers and tapered impact dampers for further investigations. Testing of an optimized tapered impact damper when subjected to the eccentric mass and motor device, showed that the device restricted the maximum vertical motion to 27% of that without the device. The maximum horizontal motion also limited to 60% of that without the device. The damper only slightly reduced the arm's movement in the horizontal direction but was very effective in bringing it to a stop quickly after wind gusts ceased [12]. Therefore, the results showed that a tapered impact damper provide the best overall potential for both vertical and horizontal damping.

Table 2
Summary of various types of damping devices investigated by Cook et al.

Device	Variation	Schematic Diagram (or General Description)	% Critical Damping	Increase
None			0.27	1.0
Tuned Mass	Traditional	Suspended Spring/Mass	8.71	32.0
	Stockbridge	Dumbbell	0.42	1.5
	Batten		1.82	6.7
Liquid	Horizontal		0.38	1.4
	U-tube		0.40	1.5
Friction			6.49	23.9
Arm-pole Connection	Belleville Spring	Beveled Washers	0.65	2.4
	Neoprene Pad	6.4 mm – 19.1 mm	No Significant	
Impact	Vertical Spring/Mass		6.79	25.0
	Horizontal Spring/Mass		0.78	2.9
	Multi-Directional Spring/Mass		No Significant	
	Spring/Mass with Liquid Impact		6.12	22.5
	Tapered Impact		4.01	14.7

McManus et al. tested various type of strut, impact and elastomeric pad dampers for 50-ft. mast arm traffic signal structure [34]. In this research the response of the first mode in-plane and out-of-plane was explored. Their findings show that the in-plane strut was significantly effective in the in-plane direction. The in-plane strut that was used in this study was comprised of a 24-ft. section connected in a series with an automobile shock absorber Figure 20. Also, the ends of the viscous damper were attached to the mast arm and to the pole extension for the luminaire. The strut was bolted to two friction-dependent collars [34].

Table 3
Damper types studied for vibration mitigation of traffic signal structures

Type of Dampers	Variation	% Critical damping	% Increase	Disadvantage (as identified by prior research)
Tuned mass damper	Traditional	8.71	32	Different natural frequency requires separate tuning
	Stockbridge	0.42	1.5	
	Batten	1.82	6.7	
Liquid damper	Horizontal	0.38	1.4	Ineffective
	U- tube	0.40	1.5	
Friction damper		6.49	23.9	Unattractive
	Pad at mast arm	0.28	1.9	
Elastomeric pads	Pad at mast arm and base	0.43	2.9	Ineffective
	Pad at base	0.39	2.6	
	Belleville Spring	0.65	0.24	
Arm Pole connection				Ineffective
Strut		2.4-6.0	16-40	Requires luminary extension
Flat bar	Unconfined	1.1	7.3	Ineffective
	1.0 s period	0.30-1.1	2.0-7.3	
	1.2 s period	0.25-0.91	1.7-6.1	
	1.4 s period	0.30-0.37	2.0-2.5	
Strand	1.0 s period	0.54-1.3	3.6-8.7	Large size and noise
	1.2 s period	0.72-1.6	4.8-10.7	
	1.4 s period	0.97-1.4	6.5-9.3	
Alcoa Dumbbell		0.26	1.7	Ineffective
Shot-put	0 degree	0.20-0.29	1.3-1.9	Ineffective
	45 degree	0.20-0.28	1.3-1.9	
Hapco		0.31	2.1	Ineffective
Impact	Vertical Spring/mass impact dampers	6.79	25	High cost
	Horizontal Spring/mass impact dampers	0.78	2.9	Ineffective
	Spring/mass liquid impact dampers	6.12	22.5	High cost
	Spring/mass liquid impact dampers	6.12	22.5	High cost
	Tapered	4.01	14.7	Unattractive



Figure 20
In-plane strut

Moreover, they concluded that the shot-put impact damper is a less feasible solution to the vibration problem of these structures. The elastomeric pads also have the fatigue problem of the anchor bolts. Besides, the strand-impact damper, in-plane strut/elastomeric pad combination, and the dual strut were the only damping systems that provided effective results in both the in-plane and out-of-plane directions. Christenson provided a table containing the damper devices that was used in the Hamilton et al., Cook et al., and McManus et al. studies to mitigate the wind induced vibration of traffic signal poles [11]. Table 3 shows a list of these dampers.

Christenson conducted an experimental study on a 35-ft. full-scale mast arm, in order to evaluate the performance of a control system to reduce the in-plane vibration of a typical cantilevered traffic signal support structure [11]. The study proposed a smart damping device placed in the signal head called signal head vibration absorber (SHVA) shown in Figure 21. The damper was designed as a magnetic damper. Therefore, signal heads themselves were allowed to translate vertically relative to the mast arm when the mast arm vibrates. Three steel plates were fixed to a steel connector between the spring and the plates. Magnets of equal strength were attached to the outer plates and a hollow aluminum tube was placed through the middle plate. Verification tests showed that the four pairs of magnets were adequate for getting a damping coefficient close to the optimal damping. This method could reduce the vibration of the structure for 98.3%. Also the SHVA was able to reduce the acceleration of the mast arm from 0.5 g to 0.06 g.

In another study, Christenson et al. conducted a field testing study of SHVAs to reduce in-plane vibration of mast arm [35]. The tests were conducted in Texas Tech University on a

signal support structure with a 60-ft. mast arm and 19.59-ft. pole. Both mast arm and pole tapered with an 18.5-in. and 21.65-in. diameter at the fixed end and 10.31-in. and 18.5-in. at the free end relatively. Based on these tests, the SHVA mitigation method was able to reduce the peak response from 4.1 in. for the structure without mitigation system at the wind speed of 10 mph to 0.37 in. and from 5.7 in. for the 16 mph wind to 0.61 in. (about 90% reduction for in-plane vibration).

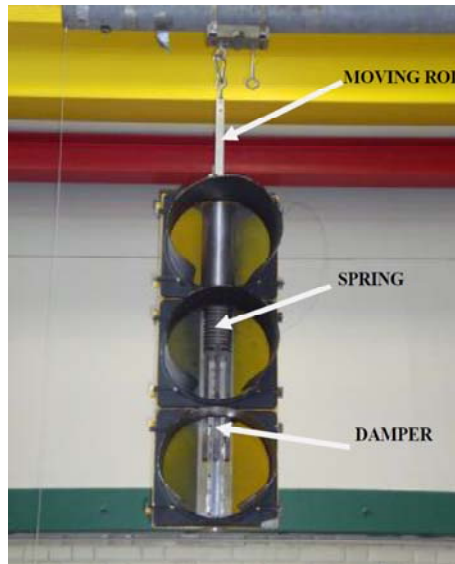


Figure 21
Smart damper (SHVA) developed by Christenson

OBJECTIVE

The main objective of the current study is to present a methodology to investigate the performance of damping devices to suppress the wind-induced vibrations in a mast arm cantilever traffic signal support structure with a circular cylinder section by using numerical tools, and validating the numerical models by conducting experimental investigations within the open-jet facility at LSU.

On this basis, the main objectives can be summarized as following:

- Using CFD with LES to create time histories of wind loads, especially lift and drag forces;
- Conducting experimental investigations to validate the numerical CFD models;
- Creating a numerical model for dynamic analysis of the structure which eventually quantify the fatigue damage due to random vibration;
- Investigating the performance of damping enhancement devices in order to improve the resiliency of the structure under wind-induced loads; and
- Extending the methodology and the results of this study to similar slender structures that are sensitive to wind-induced loads.

SCOPE

Damping enhancement in traffic lighting support structures is shown to be very effective in reducing wind-induced vibrations and stresses. The methodology, while being applicable to other types of support structures, was limited in the current study to cantilevered structures with circular and tapered poles and mast arms. Wind-induced loads on structures with different cross-sections can be different; however, the same methodology is applicable. The use of the Solidworks program, while having the potential to track stresses in the whole structure, is a very time consuming task. Accordingly, the use of other software, like MATLAB, can provide quick analysis of the dynamic behavior, provided that an accurate finite element-based model is used. The current study investigated the use of tuned mass dampers on the performance of the support structure. Future studies will investigate additional damping techniques and aerodynamic mitigation features.

METHODOLOGY

Traffic signals play a major role in the transportation field all over the world to control conflicting traffic flows, particularly at road intersections and crosswalks. A typical support structure for traffic signals is the cantilever with a single vertical pole and a horizontal mast arm. Figure 22 shows a typical cantilevered single mast arm assembly [33].

The main purpose of the this study is to present a methodology to suppress wind-induced vibrations in a mast arm cantilever traffic signal support structure with a circular cylinder section by using numerical tools (CFD with dynamic modeling), and validating the numerical models by conducting experimental investigations at the open-jet facility at Louisiana State University (LSU).

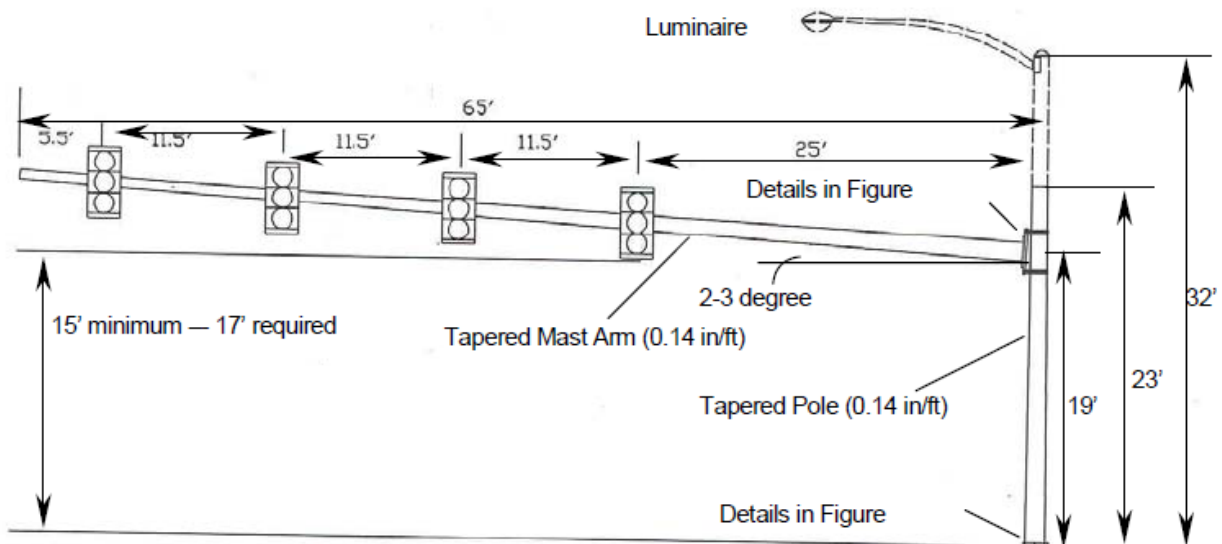


Figure 22
Typical single mast arm and pole assembly

First, the aerodynamic characteristics of the structure were investigated by employing a transient RSM 2-D CFD model. Second, the model was validated by experimental testing. After making sure that the CFD model was capable of simulating flow patterns and vortex shedding effects for this type of structures, a more elaborated 3-D CFD model was implemented by using a time dependent approach LES scheme. The model was run on LSU HPC clusters to expedite the simulations. Monitoring points were defined on the mast arm to capture pressure coefficients, and hence to calculate the lift and drag forces on the structure at different sections, for better accounting for wind load distribution.

Finally, the simulated wind-induced loads were used in a dynamic model in to evaluate the influence of three dampers in order to reduce vibrations and hence stresses in the traffic lighting support structure. The performance of the dampers was investigated by comparing the displacement of the mast arm and the stresses developed in the structure for both controlled (with dampers) and uncontrolled (without dampers) cases. It is aimed that the methodology and the results of the current study can be extended to investigate the performance of different damping enhancement methods for traffic lighting support structures, as well as for similar slender structures that are sensitive to wind-induced loads.

Modeling of Hurricane Loading on a Traffic Lighting Support Structure

CFD simulations are capable of providing a better understanding of wind engineering aspects of very complex flows around the structures. Computational wind engineering (CWE) in civil engineering covers a wide range of aerodynamics problems from the effects of wind on low-rise buildings to high-rise skyscrapers, and from the suspended cable bridges to the complex industrial facilities. Being armed with the CFD tools, it would be possible to simulate the complex flow fields and aerodynamic characteristics of these diverse structures. The target structure which is studied in this research is considered as a unique structure that the Reynolds number plays a critical rule in defining flow field around the body.

There are several numerical and experimental studies on the aerodynamic characteristics of structures with circular cylinder sections in different flow regimes. Among other parameters that govern the flow patterns and define the flow field distribution around a bluff body with a curved shape, including circular cylinders, and hence wind induced loads, Reynolds number is an important parameter. Reynolds number is the ratio of fluid inertia forces to the viscous forces, which can be used to define the separation points on a circular cylinder. In the case of bluff bodies with sharp edges, the separation points are not so dependent on the Reynolds number. For the experimental part, Bursnall and Loftin investigated the pressure distribution on a circular cylinder at various yaw angles near and above the critical Reynolds numbers [36]. Roshko investigated the flow characteristics past a circular cylinder at high Reynolds number [37]. Achenbach and Heinecke studied the effect of surface roughness on the frequency of vortex-shedding in circular cylinders [38]. Raghavan and Bernitsas conducted experimental investigations on the effect of Reynolds number on vortex induced vibrations (VIV) of rigid circular cylinder on elastic support [39]. They concluded that there is a strong dependence of VIV response on Reynolds number. Belloli et al. studied VIV at high Reynolds numbers, using an experimental set-up which allows to reach Reynolds numbers up to 6×10^5 [40]. They measured pressure distributions, and aerodynamic coefficients together with model displacements for a circular cylinder.

Reynolds number causes issues that make it difficult to experimentally simulate turbulence around a bluff body in field measurements or even in a laboratory. These difficulties mainly come from the limitations in visualizing the complex 3-D flow around the bluff body in details. Therefore, the need for an elaborated CFD simulation will be more highlighted, as it is possible to cover Reynolds issues and define various scenarios to capture the aerodynamic characteristics of the structure in a controlled manner in a CFD model. The main shortcoming of CFD comes from the high computational cost which arises by implementing sophisticated numerical models. Considering all the aspects, it is important to work on the approaches which can eventually lead to minimizing the computational costs, while improving the accuracy of the results. On this basis, this research is aimed at investigating the aerodynamic characteristics of a mast arm cantilever traffic signal support structure by implementing elaborated numerical tools and validating them against the experimental results which was conducted at the open jet facility at LSU. The methodology of this research can also be extended in the case of other similar structures to model the aerodynamic characteristics.

For the numerical part, there are different techniques to simulate 3-D unsteady flow around structures with circular cylinder section. The most widely used approach in recent years was based on solving the Reynolds Averaged Navier-Stokes equations (RANS). RANS models present time-averaging results for the turbulence characteristics of the flow, which alleviate the cost of the computation. However, this methodology is not capable of yielding satisfying and accurate results in the case of vortex-dominated problems, especially in the rear part of a bluff body. As a solution, Direct Numerical Simulation (DNS) and LES were developed in order to cover the unsteady problems.

In this study, the aerodynamic characteristics of a mast arm cantilever traffic signal support structure with a circular cylinder section was simulated and investigated by CFD simulations. By implementing the 2-D RSM and the 3-D LES schemes, a time-dependent approach was followed. Monitoring points were defined on the mast arm to capture the pressure coefficients, and hence to calculate the lift and drag forces on the body. The simulated time histories of drag and lift forces were used for the control purposes in dynamic modeling. As a result, appropriate alternatives will be recommended in order to mitigate the wind induced vibrations of these types of structures; the alternatives can be defined as aerodynamics optimization recommendations and/or structural controls strategies. Although there are some field measurements of wind effects on traffic light support structures, similar to the study carried out in reference Christenson et al., there are always difficulties and uncertainties in capturing the real wind loads and responses of the structure during hurricanes and other types

of windstorms in the field [35]. On this basis, it is essential to go back to the laboratory and utilize the numerical and experimental tools which make it possible to investigate various aspects of the problem to examine the factors of which their effects are not yet fully understood.

In this study, the same dimensions for the traffic support structure described in Christenson et al. were used [35]. The paper presented a field testing which was conducted at Texas Tech University's National Wind Institute Wind Engineering Research Field Laboratory. The traffic signal support structure has a mast arm length of 60-ft. (18.29-m), as shown in Figure 23 [35]. The traffic pole is a mono-tubular pole and a cantilevered arm with a circular cross section. The 19.59-ft. (5.97-m) pole is tapered with a 21.65-in. (0.55-m) diameter at the base and an 18.5-in. (0.47-m) diameter at the top. The 60-ft. (18.29-m) mast arm has an 18.5-in. (0.47-m) diameter at the mast arm-to-pole connection and a 10.31-in. (0.262-m) diameter at the free end of the mast arm.



Figure 23
Field test of 60-ft. mast arm with vertically mounted signal heads

In order to simulate the model in CFD, first a 2-D computational model was created and examined in ANSYS FLUENT. The main reason for using this 2-D model was to investigate the accuracy of CFD models in flow simulation and vortex shedding modeling for this special geometry shape support structure, and afterwards to examine the numerical results with similar conditions in a laboratory test. To achieve this goal, the methodology of CFD simulation in 2-D will be presented, and afterwards the experimental set up and various laboratory tests will be discussed, and finally the methodology implemented to simulate the elaborated 3-D model and corresponding results will be presented.

2-D Numerical CFD Model

In order to simulate the model in CFD, a 2-D computational model was developed in ANSYS FLUENT. A structured mesh was initially created in ICEM. Figure 24 shows the computational domain and the variable mesh sizes within the domain near the walls, i.e. around the circle and near the ground. As indicated in the figure, a finer mesh was adopted near the wall regions in a way that the flow details can be better captured without needing to refine the whole domain. The finest mesh was around the circular cylinder where flow separation and vortex shedding are expected, and therefore the need for a high resolution mesh size. Similarly, near the ground another finer mesh size was applied as can be seen in Figure 24 left.

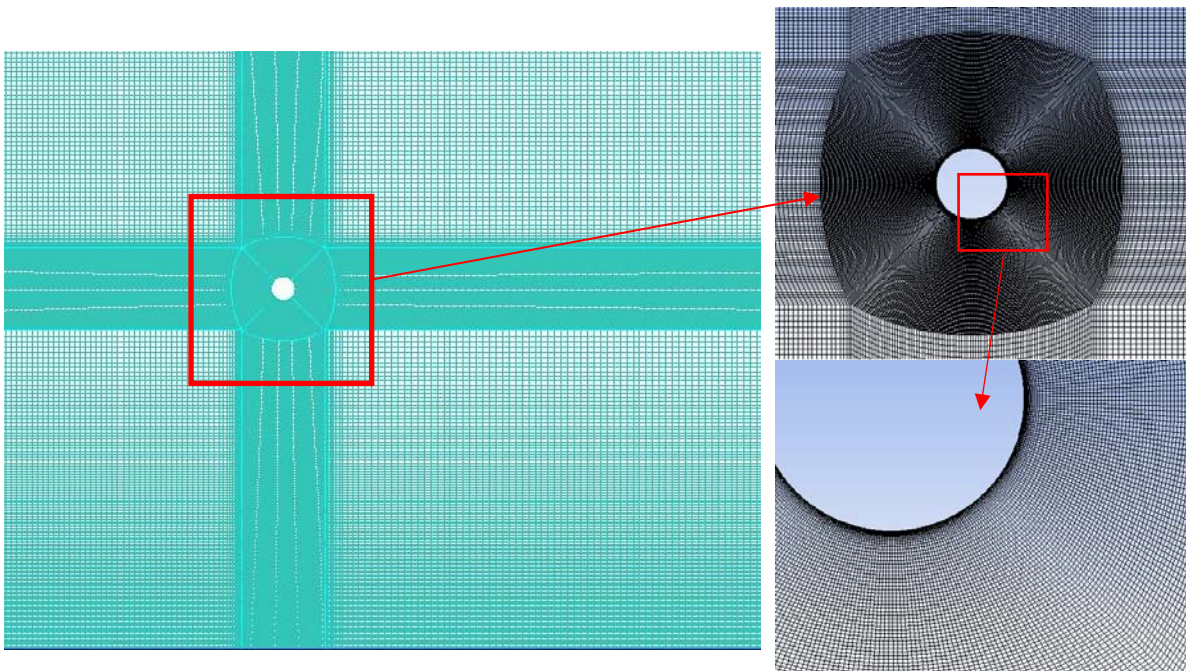


Figure 24
2-D domain for CFD analysis and structured mesh with finer mesh sizes

The boundary condition at the upper surface was “symmetry,” and for the outlet a “pressure outlet” was applied. The inlet wind velocity profile is a uniform profile for this 2-D case. For the ground, and the circular cylinder, a “wall” condition was applied. In order to decide what mesh size is the best one, a mesh independence study was conducted, and therefore four various mesh files were produced. In Table 4, the details of each case for the mesh independence study are presented.

Table 4
Various cases for mesh independence study

Case	Number of Cells
1	81K
2	205K
3	468K
4	833K

Because the main idea of 2-D CFD simulation was to catch the vortex shedding effects, a transient analysis was used by implementing RSM scheme in FLUENT, and then the results were compared with experimental results. The Reynolds Stress Model (RSM) is one of the most capable turbulence model which is available in FLUENT. RSM closes the RANS equations by solving transport equations for the Reynolds stresses, together with an equation for the dissipation rate. This feature enables the scheme to solve five additional transport equations that are required in 2D flows and seven additional transport equations which are being solved in 3D flows. The exact form of transport equations for the transport part of the RSM, $\overline{\rho u'_i u'_j}$ can be expressed as follows [41] and [42]:

$$\begin{aligned}
 & \underbrace{\frac{\partial}{\partial t}(\overline{\rho u'_i u'_j})}_{\text{local time derivative}} + \underbrace{\frac{\partial}{\partial x_k}(\overline{\rho u'_k u'_i u'_j})}_{\text{convection}} = - \underbrace{\frac{\partial}{\partial x_k} \left[\overline{\rho u'_i u'_j u'_k} + p(\delta_{ij} u'_i + \delta_{ik} u'_j) \right]}_{\text{turbulence diffusion}} + \underbrace{\frac{\partial}{\partial x_k} \left[\mu \frac{\partial}{\partial x_k} (\overline{u'_i u'_j}) \right]}_{\text{molecular diffusion}} \\
 & - \underbrace{\rho \left(\overline{u'_i u'_k} \frac{\partial u'_j}{\partial x_k} + \overline{u'_j u'_k} \frac{\partial u'_i}{\partial x_k} \right)}_{\text{stress production}} - \underbrace{\rho \beta (g_i \overline{u'_j \theta} + g_j \overline{u'_i \theta})}_{\text{buoyancy production}} + \underbrace{p \left(\frac{\partial u'_i}{\partial x_j} + \frac{\partial u'_j}{\partial x_i} \right)}_{\text{pressure strain}} - \underbrace{2\mu \frac{\partial u'_i}{\partial x_k} \frac{\partial u'_j}{\partial x_k}}_{\text{dissipation}} \quad (12) \\
 & - \underbrace{2\rho \Omega_k (\overline{u'_j u'_m} \varepsilon_{ikm} + \overline{u'_i u'_m} \varepsilon_{jkm})}_{\text{production by system rotation}} + \underbrace{S_{\text{user}}}_{\text{user defined source term}}
 \end{aligned}$$

In the solution methods' box, SIMPLE scheme was selected for the pressure-velocity coupling, and a second order implicit scheme was imposed for the transient formulation with a time step of 0.001 s, and maximum 20 iterations in each time step.

In CFD simulations, a converged solution means that the results produced by the software are accurate enough, and matched to the physical aspects of the problem based on the boundary conditions that are defined in the beginning of the simulation. As a general rule, a 3-5 orders

of magnitude of convergence is an accepted range for most of the problems. Sometimes, the iterations may not yield very low residuals, but the values are not changing significantly while advancing the iterations. In this case, we may accept the results as a converged solution. If the solutions are not converged, one needs to keep the simulations running, until there is no big change in the residuals.

Figure 25 represents the distribution of mean pressure coefficient around the cylinder for 4 CFD RSM cases in 2-D domain with various cell numbers in flow velocity of 19.95 mph and the diameter of 0.14 in. As it is seen, there is no major differences between the various cases which were investigated for the mesh independence study in terms of pressure distribution around the body. On this basis, in order to make a balance between computational costs and the mesh resolution, the mesh file with 468K cells was selected as the main case file to be analyzed and compared with experimental results for investigation of Reynolds number effect.

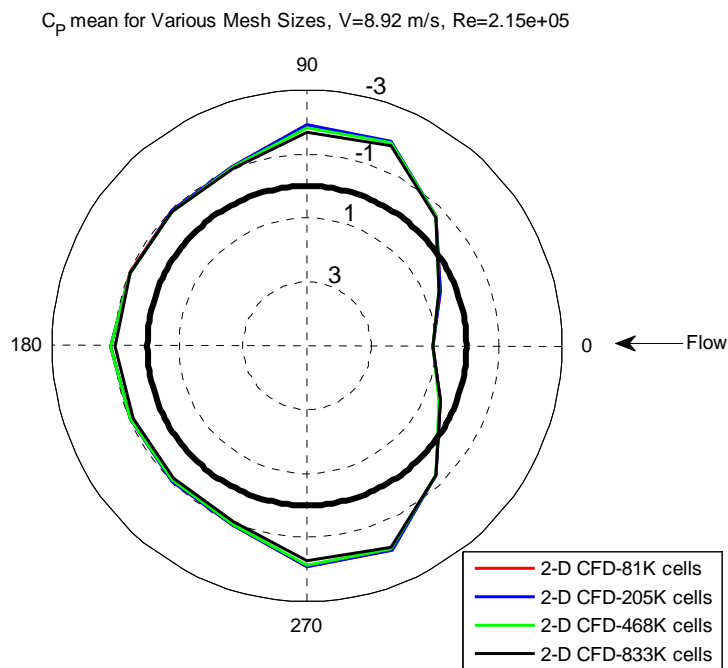


Figure 25

Distribution of mean pressure coefficient around the cylinder for 4 CFD RSM cases

From Figure 25 it is seen that the mean pressure distributions have a symmetric pattern about the x-axis (the line from $\theta = 0$ to $\theta = 180$ degrees). It means that the lift forces which are a resultant of the difference of pressure distributions on the upper and the lower sides of the cylinder will have a mean value around zero. Although the value of the lift force is important for us, the time variation of the lift forces are much more crucial in the fatigue analysis of the

support structure which are achievable from the simulation. In contrast to the pressure distributions on the above and the lower sides, the pressure distributions in front and the aft of the cylinder are not symmetric, so the calculation may yield bigger mean drag forces in compare to the mean lift forces.

Figure 26 represents the lift coefficient (C_l) history for the RSM 2-D case with 468 K cells and flow velocity of 14.47 mph. It is shown that after the transient part which is around 2 second passed from the beginning of simulation, the time history of C_l reaches to a steady state condition. It means that the vortex shedding is fully developed and therefore vortex-induced fluctuation of lift forces during the simulation time can be observed.

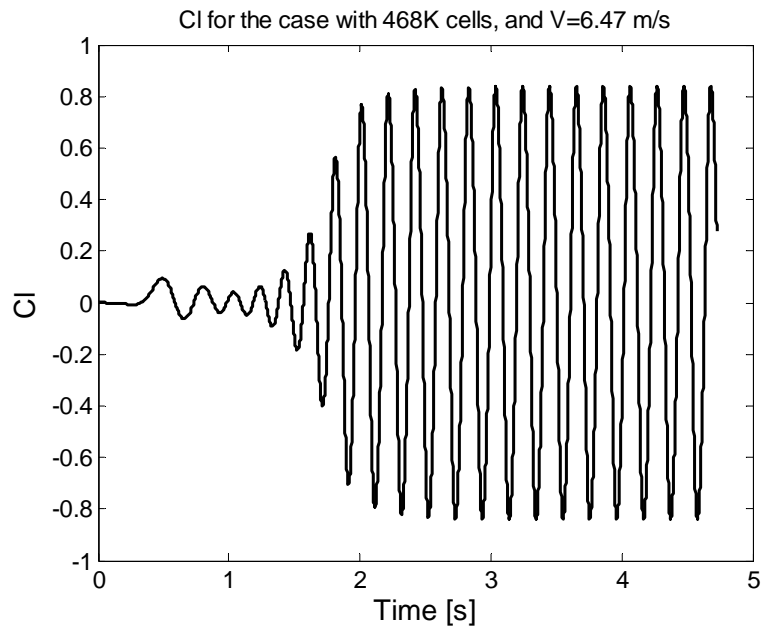


Figure 26

Lift coefficient history for the RSM 2-D with 468 K cells and flow velocity of 14.47 mph

Figure 27 represents the history of the drag coefficient for the RSM 2-D case with 468 K cells and flow velocity of 14.47 mph. It is also shown that after the transient part, which is around 2 second passed from the beginning of simulation, the time history of C_d reaches to a steady state condition.

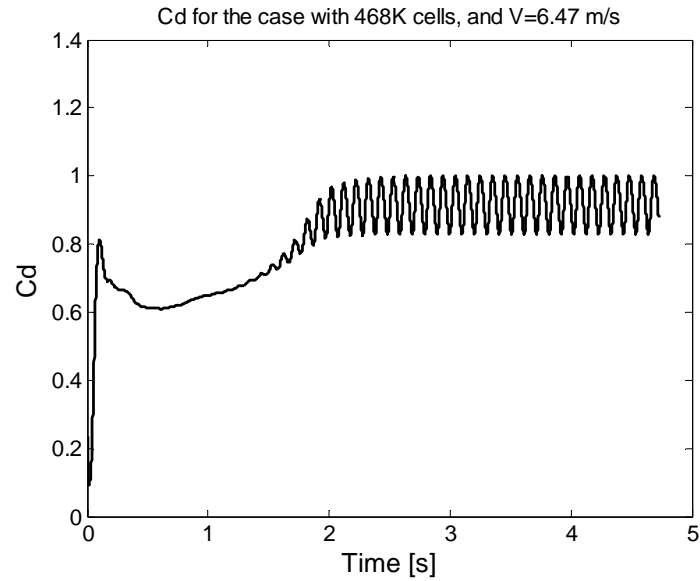


Figure 27
Drag coefficient for the RSM 2-D with 468 K cells and flow velocity of 14.47 mph

The power spectrum density of drag and lift coefficients for the RSM 2-D case with 468 K cells and flow velocity of 14.47 mph are shown in Figure 28. It can be seen that there is one peak for drag and two peaks for the lift coefficients. These peaks are related to vortex shedding, and it is possible to estimate the frequency of vortex shedding from the correspondence values in horizontal axes. Based on the diagram, the frequency of vortex shedding is equal to 4.88 Hz which corresponds to the first peak in power spectrum related to lift coefficient.

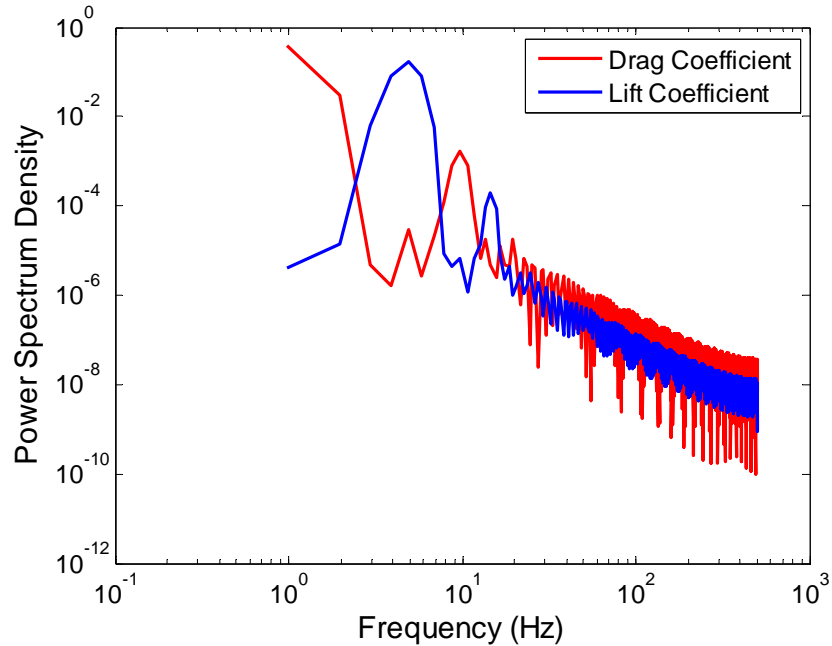


Figure 28
Power spectrum density for drag and lift coefficients for the RSM 2-D case

Finally, Figure 29 shows the distribution of the mean pressure coefficient around the cylinder for 4 CFD RSM cases in 2-D domain with 468K cells and 4 various velocities for a circular cylinder with diameter of 0.14 in. The main aim of this comparison is to investigate the effect of Reynolds number. It can be observed that for the Reynolds number ranges of $3.94e+04$ to $9.94e+04$, there is no significant difference in non-dimensional pressure coefficient around the body. It is worthy to mention that when a very high velocity of 50 m/s is examined, there are changes in the pressure distribution patterns above and below of the cylinder. The Reynolds number is equal to $1.21e+06$ in that case. It is also worth noting that in front of the cylinder where the stagnation point is located (where $V = 0$), the pressure coefficient at this point in an incompressible flow, is always equal to 1.0. This is the highest allowable value of C_p anywhere in the flow field. Note that for a compressible flow, C_p at stagnation point is greater than 1.0. It is also learnt from Figure 29 that in regions of the flow where $V > V_\infty$ or $p < p_\infty$, C_p will be a negative value as it is seen in top, bottom, and back of the cylinder.

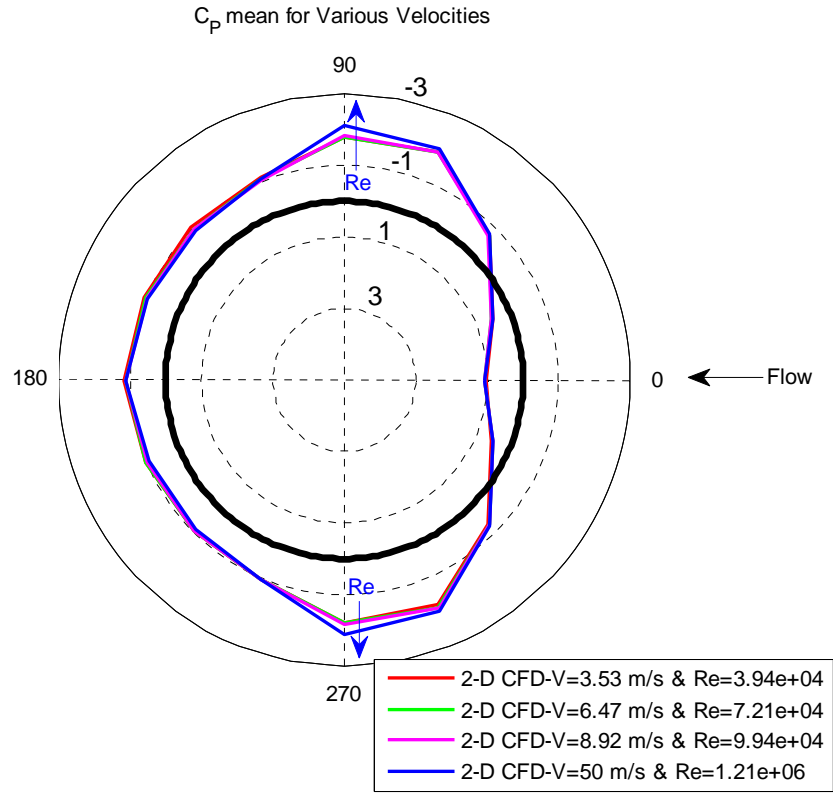


Figure 29
Distribution of mean pressure coefficient around the cylinder for 4 CFD RSM cases

Experimental Study of the Model

After creating the transient RSM 2-D CFD model in ANSYS FLUENT, the model was validated against the experimental tests which were undertaken within the open jet facility at LSU. There are some advantages in using open jet facilities instead of using wind tunnel, which were the main motivation to undertake the tests in an open jet facility. As it is known, wind tunnel is a device for producing airflow to the body under test which can provide uniform flow conditions in their test section. Figure 30 shows LSU's wind tunnel with its boundary-layer test section and flow conditioner part [43].

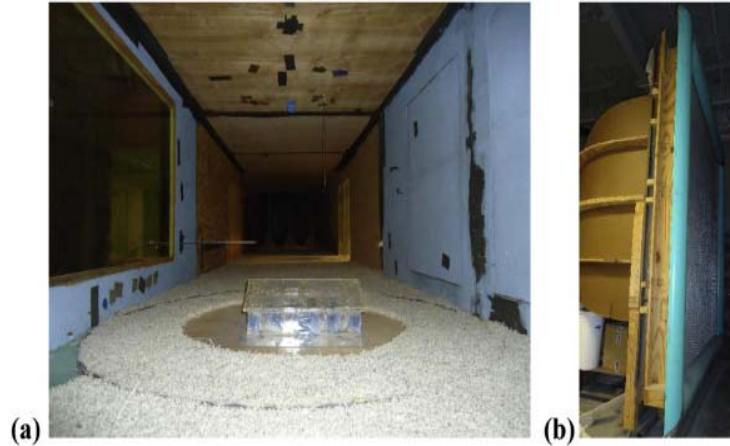


Figure 30
LSU's wind tunnel: (a) boundary-layer test section; (b) flow conditioner

It should be noted that there are some shortcomings in the application of wind tunnel in the cases of low rise buildings, energy infrastructures, and small-sized structures, which are mainly due to the lack of capability to simulate turbulence in the wind tunnel at an appropriate large scale. Another challenge for the small size wind tunnel is that the Reynolds number would be far different from the one in nature. These challenges ignited the idea to implement open jet facilities in this study in order to examine the aerodynamic characteristics of traffic light support structure. As an advantage, destructive testing at a very high wind speeds are possible which means that the issue with Reynolds number would be greatly improved. Figure 31 represents the main concept of the open jet testing, and the one which is constructed and under test within the LSU WISE research group [43].



Figure 31
Open-jet simulations: (a) main concept (b) small-scale open-jet simulator at LSU

In order to conduct the experiments, two samples were selected and five different scenarios were tested with variation in wind velocity to obtain various Reynolds numbers. Figure 32 shows the schematic representation of the circular cylinder geometry and the domain dimensions for both cases 1 and 2.

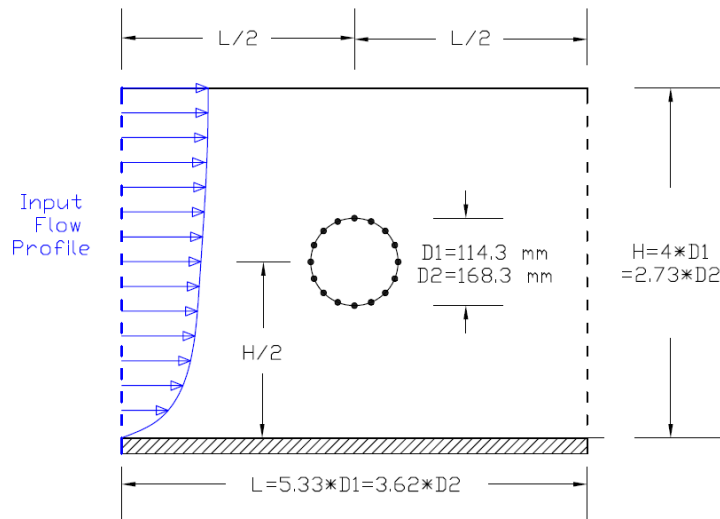


Figure 32
Schematic representation of the circular cylinder geometry and the domain

Table 5
Diameter, wind speed, and Reynolds number for each experimental cases

Case	Diameter (mm)	Mean Wind Speed (m/s)	Reynolds Number
1	114.3	8.74	6.61e+04
2	114.3	4.80	3.63e+04
3	168.3	8.92	9.94e+04
4	168.3	6.48	7.21e+04
5	168.3	3.53	3.94e+04

Figure 33 shows the procedure of experimental set up, and connecting the pressure measurement probe to the tube which are intended to yield the time history of pressure distribution over the circular cylinder during the test. For each sample, 16-tap pressure scanners which are located along the cylinder centerline were used in order to monitor and

obtain the distribution of the simultaneous time varying surface pressure on the circular cylinder body.

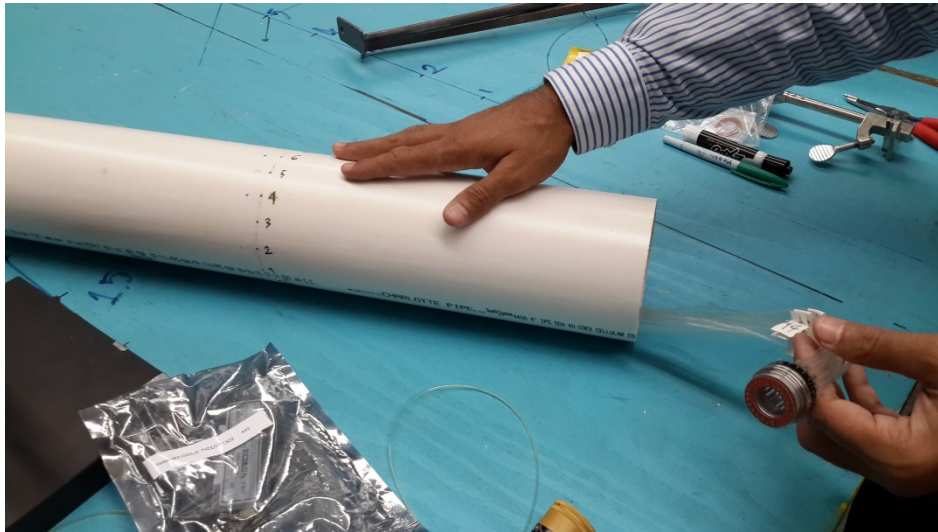


Figure 33

The experimental set up and connecting the pressure measurements sensors

The first model with $D = 4.5$ in. can be seen in Figure 34, and the second model with $D = 6.63$ in. is shown in Figure 35.

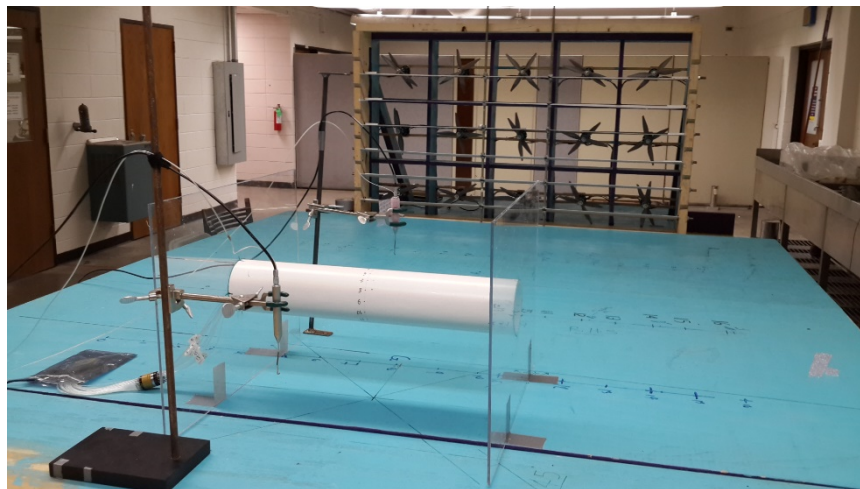


Figure 34

Experimental setup for the first model with $D = 4.5$ -in.

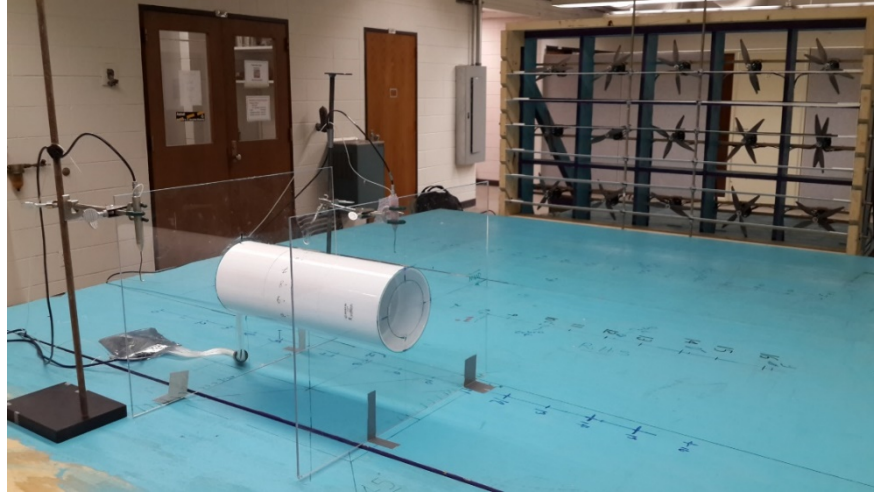


Figure 35
Experimental setup for the second model with $D = 6.63$ in.

Figure 36 shows a general view of the open jet facility and detailed pictures of the devices which were used in order to record and process the time history of pressure and velocity measurements within the monitoring points during the tests. Figure 36-1 shows the general view of the open jet facility. Figure 36-2 is the model in front of the flow; Figure 36-3 is the Cobra probe used for measuring mean and fluctuating 3-component velocities and static pressure; Figure 36-4 shows ZOC23b miniature pressure scanner, and Figure 36-5 is the computer and software installed on it to process and record the time history of pressure and velocities within the monitoring points.

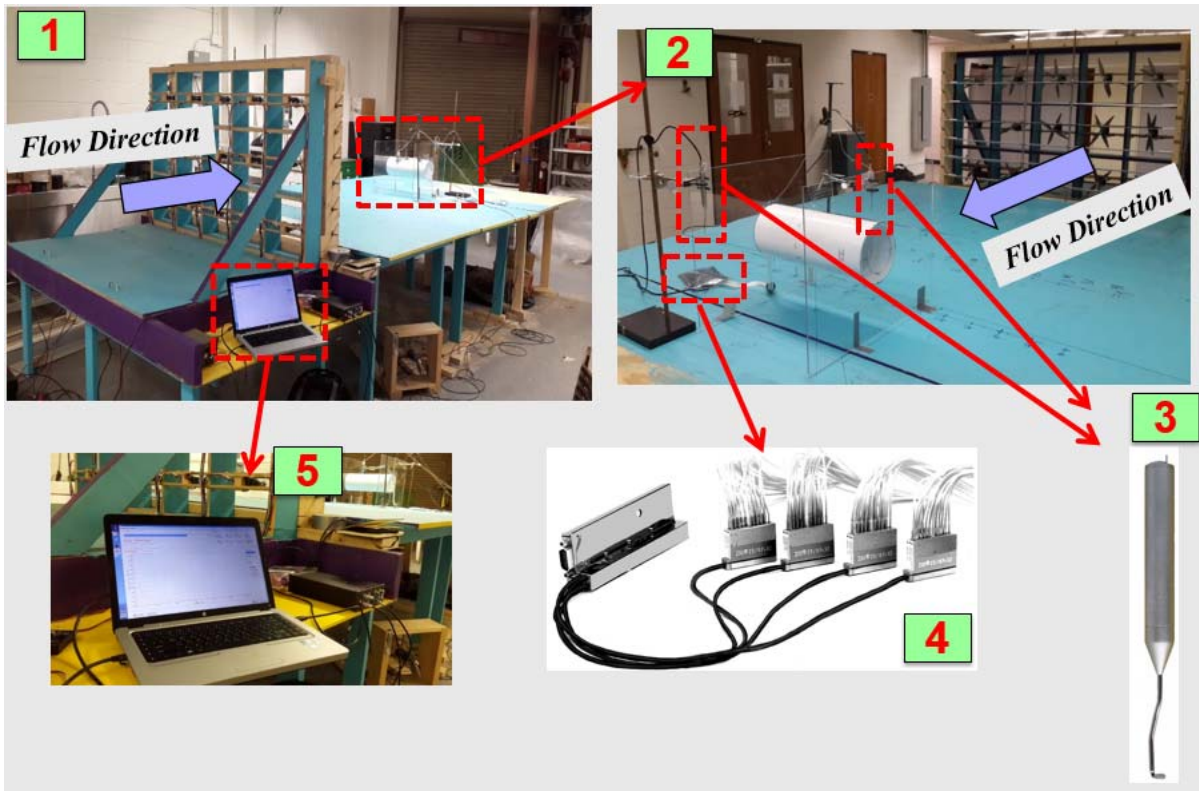


Figure 36
Experimental setup

As can be seen in Figure 36, the Cobra Probe was used to monitor the free stream velocity and the pressure differences before and after the structure. The Cobra Probe is a dynamic multi-hole pressure probe for measuring mean and fluctuating 3-component velocities and static pressure in real time. It provides frequency response from 0 Hz (mean value) to more than 2 kHz. It comes fully calibrated and does not need recalibrating other than occasional checking of the voltage-to-pressure scaling (static calibration). One of the disadvantage of Cobra Probe is that the Cobra Probe has a lower potential frequency response (0 to > 2 kHz) than that of hotwires, and is limited to flow speeds that are greater than 2 m/s (turbulantflow.com).

It is also seen in Figure 36 that a miniature pressure scanner is used to measure air pressure induced from the 16-tap pressure scanners along the cylinder centerline. The ZOC23b miniature pressure scanner (32Px) is designed to measure gas pressures only. The pressure sensor and calibration valves are divided into 4 remote modules, each containing 8 pressure sensors. The 4 remote pressure sensor modules are connected with electrical umbilical which connect into the ZOC23b amplifier multiplexer unit. Each module has its

own reference pressure, calibration tabulations, and calibration valuing. This allows the remote pressure sensor modules to be different pressure ranges [44].

Table 6 represents the results of various experimental tests.

Table 6
The results of experimental tests

	Diameter (m)	Velocity before the structure (m/s)	Velocity after the structure (m/s)	Length Scale	Velocity Scale	Frequency Scale	Vortex Shedding Frequency (Hz)	Strouhal Number	Reynolds Number
Case 1	0.1143	8.74	6.95	3.19	1.8570	1.7197	18.84	0.25	6.61e+04
Case 2	0.1143	4.80	3.15	3.19	3.3805	0.9446	8.02	0.19	3.63e+04
Case 3	0.1683	8.92	8.75	2.17	1.8192	1.1922	14.94	0.28	9.94e+04
Case 4	0.1683	6.48	6.07	2.17	2.5062	0.8654	10.19	0.27	7.21e+04
Case 5	0.1683	3.53	2.56	2.17	4.5921	0.4723	4.53	0.22	3.94e+04

Figure 37 shows the distribution of the mean pressure coefficient around the cylinder for 3 experimental cases with various velocities, low, medium, and high velocity values for the model with diameter of $D = 6.63$ in. The corresponding Reynolds numbers are also listed in the figure. It can be seen that the general trend for all cases are similar, although by increasing the Reynolds number the pressure clouds are changing.

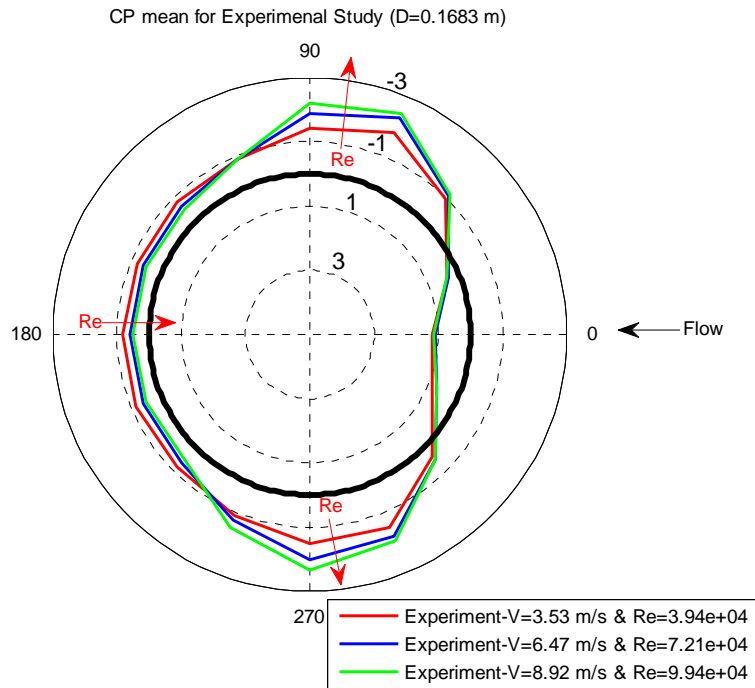


Figure 37
Distribution of mean pressure coefficient around the cylinder for 3 experimental cases

Considering Figure 37, it is seen that in front of cylinder (at stagnation point where the velocity of flow is zero) $C_p = 1$. This value is always consistent at a stagnation point in an incompressible flow. Therefore, it can be interpreted that at stagnation point, or the local pressure is “one times” the dynamic pressure above freestream static pressure. For regions that $C_p = -2$, then $p = p_\infty - 2q_\infty$, or the local pressure is three times the dynamic pressure below freestream static pressure.

Similar to Figure 37, Figure 38 shows the distribution of mean pressure coefficient around the cylinder for two experimental cases with various velocities, low, and high velocity values for the model with diameter of $D = 4.5$ in. The corresponding Reynolds numbers are also listed in the figure. It can be seen that the general trend for the two cases are similar. It is also seen that by increasing the Reynolds number the pressure clouds are changing in a similar fashion. The rate of change is more considerable in top and bottom of cylinder in comparison to the back of cylinder.

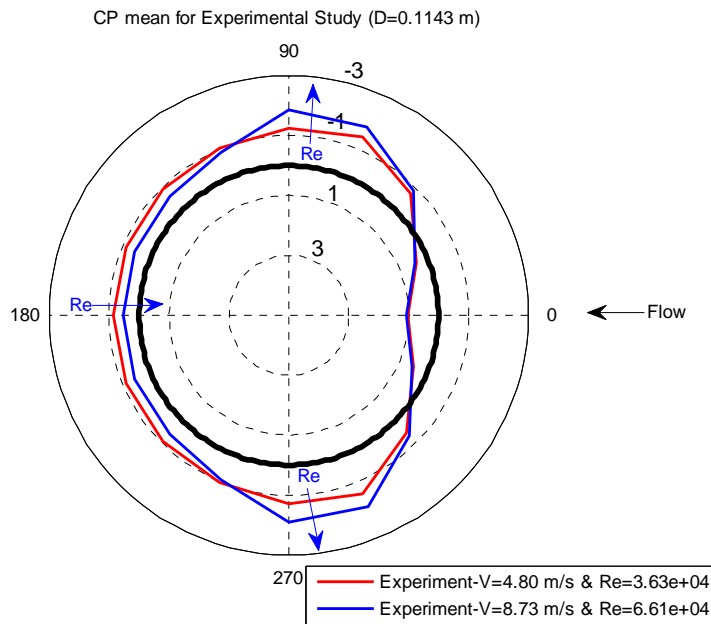


Figure 38

Distribution of mean pressure coefficient around the cylinder for 2 experimental cases

Comparison between CFD and Experiment Results

In order to validate the 2-D computational model, in this part a comparison between the numerical and the experimental results is presented.

Figure 39 shows the distribution of mean pressure coefficient around the cylinder for two cases, the 2-D RSM CFD model with the low velocity of $V = 7.9$ mph, $D = 14.37$ in., $Re = 8.53e+04$, and 468K cells. For the experimental part, the same velocity is simulated, but with different diameter of $D = 6.63$ in. which resulted in a new Reynolds number as $Re = 3.94e+04$.

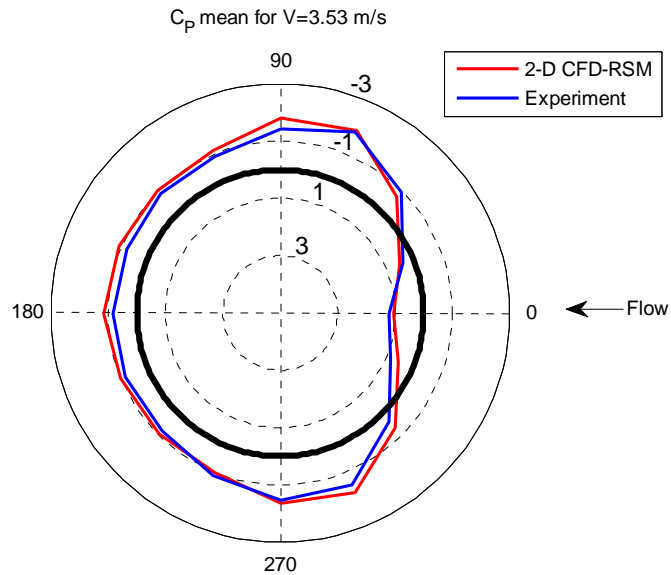


Figure 39
Distribution of mean pressure coefficient around the cylinder for 2 cases

A similar comparison is done for the medium flow velocity as can be seen in Figure 40. It shows the distribution of mean pressure coefficient around the cylinder for 2 cases, the 2-D RSM CFD model with the medium velocity of $V = 14.47$ mph, $D = 14.37$ in., $Re = 1.56e+05$, and 468K cells. For the experimental part, the same velocity is simulated, but with different diameter of $D = 6.63$ in. which resulted in a new Reynolds number as $Re = 7.21e+04$.

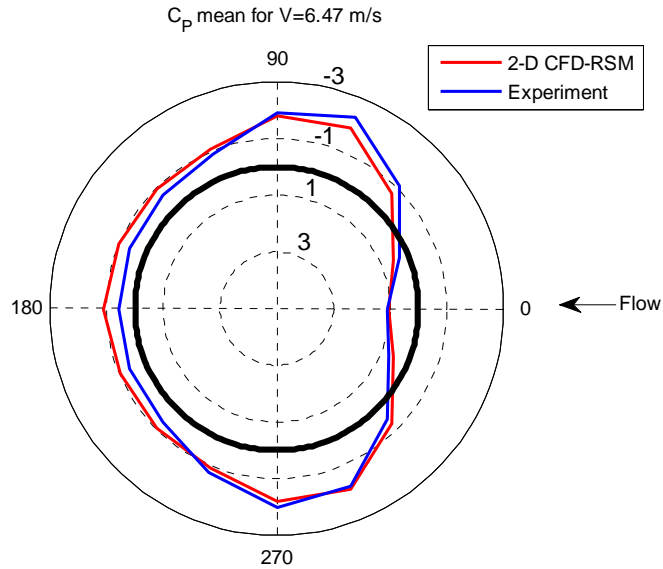


Figure 40
Distribution of mean pressure coefficient around the cylinder for 2 cases

Finally, the results of numerical and experimental simulations for high wind speed are compared in Figure 41. The figure represents the distribution of mean pressure coefficient around the cylinder for 2 cases, the 2-D RSM CFD model with the medium velocity of $V = 19.95$ mph, $D = 14.37$ in., $Re = 2.15e+05$, and 468K cells. For the experimental part, the same velocity is simulated, but with different diameter of $D = 6.63$ in. which resulted in a new Reynolds number as $Re = 9.94e+04$. Figure 42 also shows Spectra of the wind velocities upstream (input velocity spectrum) and downstream (vortex shedding spectrum), indicating a vortex shedding frequency of 8.16 Hz that corresponds to a Strouhal number of 0.21.

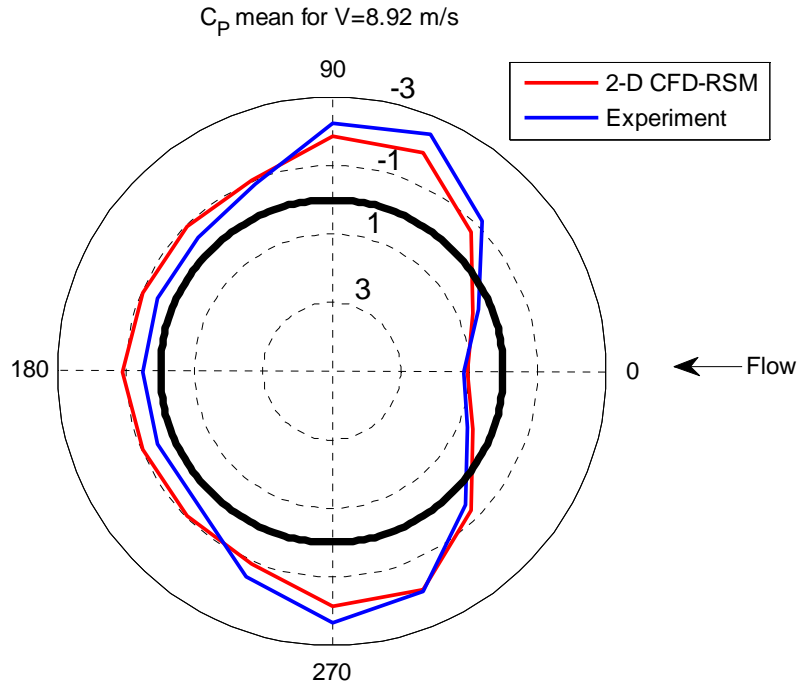


Figure 41
Distribution of mean pressure coefficient around the cylinder for 2 cases

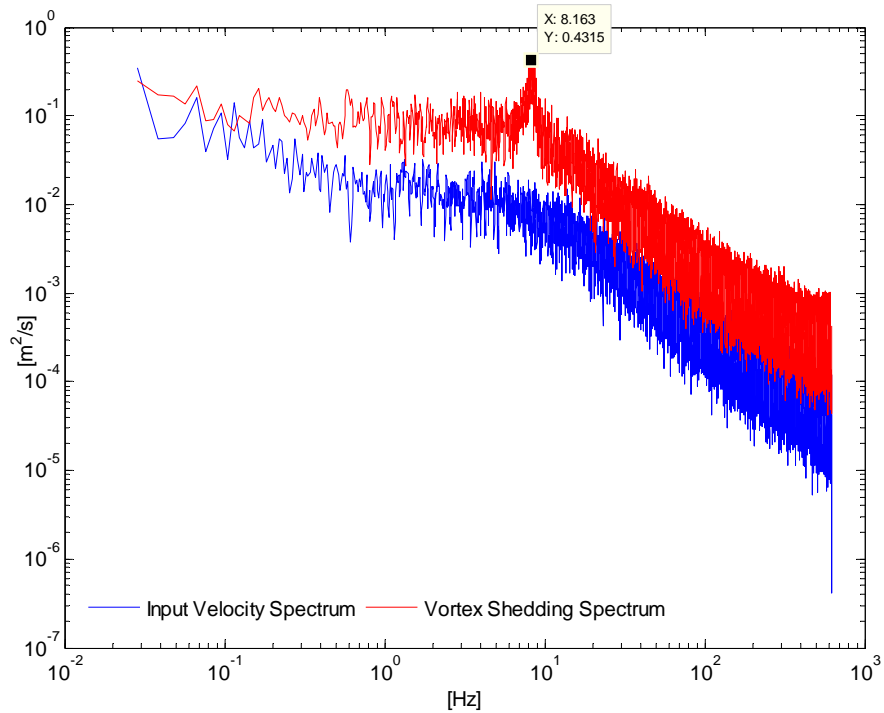


Figure 42
Spectra of the wind velocities upstream and downstream

3-D CFD Simulation of the Model

After making certain that the 2-D CFD model is in a good agreement with the experimental tests, and the results are satisfactory, a detailed 3-D CFD was created in order to investigate the aerodynamic characteristics of the structure as realistic as possible. To this aim, the geometry of traffic light support structure which is introduced by Christenson et al. [35] is first created in the AutoCAD and then exported to the ICEM CFD for generating the meshed domain [45]. Using the ICEM CFD, the meshes were created and exported as unstructured mesh (.msh) file that can be read by the ANSYS FLUENT software. Then the CFD model was investigated in FLUENT for the conditions well matched with the real life of the structures with full scale in the field. The methodology that was used for aerodynamic study of the 3-D model is illustrated in Figure 43.

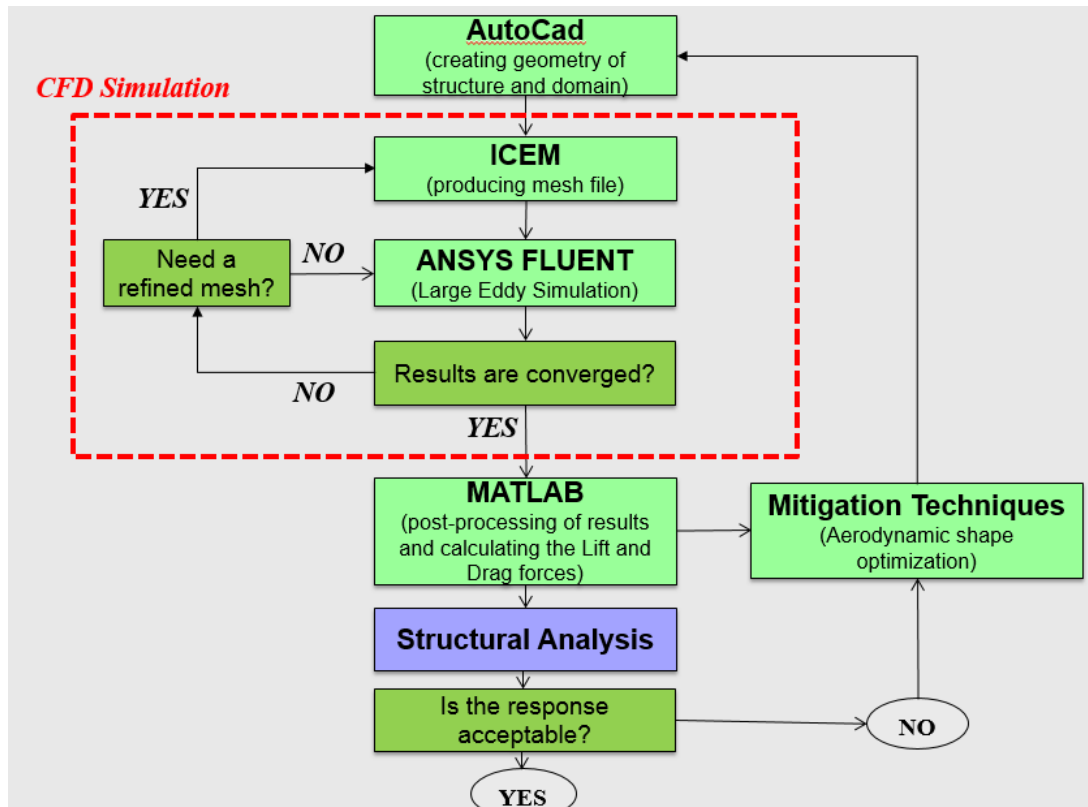


Figure 43

The methodology used for the 3-D aerodynamic analysis of traffic support structure

It can be seen that after CFD simulations, the results are being post-processed, resulting in aerodynamic forces which can be used as input for the structural analysis. Meanwhile, mitigation techniques can be implemented in order to suggest aerodynamic optimization and also structural solutions for a better performance of the structure under the random wind loads.

Boundary Conditions and Meshing Procedure

Figure 44 (a) represents a general view of the 3-D domain and the dimensions which are defined in ICEM to create the mesh file to be used in FLUENT for CFD analysis. At this stage, it is crucial to define the best appropriate conditions for the boundaries of the problem. The boundary condition at the upper surface and at the two sides of the domain is “symmetry” condition, and for the outlet a “pressure outlet” is applied as well. The inlet turbulence parameters and the wind velocity profile are defined by a UDF to the FLUENT. For the ground, arm, and the pole, a “wall” condition was applied accordingly.

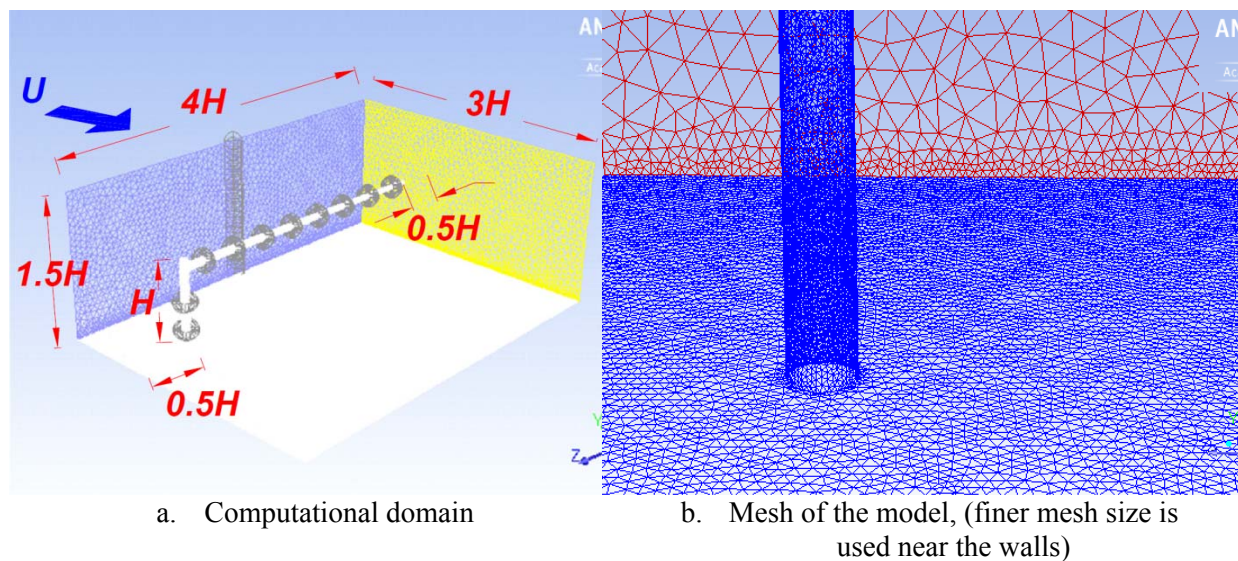


Figure 44

Mesh generated computational domain

A combined tetra/prism meshing procedure was applied for the volume region surrounding the structure. Defining a finer prism mesh region around the walls made it possible to produce finer mesh, and as a result, flow details will be better captured without needing to refine the whole mesh. On this basis, the finest mesh size in our model is applied to the arm and pole of the support structure. A coarser mesh is applied for the ground with maximum. And the coarsest mesh is imposed to the other parts of the domain as well. The total number of cells of the domain is 1.79 m, with a total number of grid nodes equals to 346544. The various mesh sizes are shown in the Figure 44 (b).

Turbulence Model Used for the Simulation

There are three main approaches for dealing with fluid computational problems including, RANS models, LES, and DNS. RANS models solve the time-averaged Navier-Stokes equations which is the most widely used approach for simulation the flows in industry. In contrast, LES is a transient and time-varying turbulence model that is placed between the

RANS and DNS models based on the accuracy of the results. Although LES yields improved accuracy in comparison to the RANS models, the large computational time and cost are the main disadvantages of the LES approach. To cope with this issue, hybrid approach of RANS+LES was developed which is known as Detached Eddy Simulation (DES) [46]. DNS solves the full Navier-Stokes equations, instantaneously in time and three-dimensional space. It requires a very high time and computational cost, therefore is not applicable for the industrial flows and practical cases.

In this study, for structural evaluation and fatigue analysis, time histories of wind-induced forces are required to simulate the dynamic responses of the structure. Therefore, it was essential to simulate the unsteady flow patterns around the structure in order to simulate the turbulence and capture the peak wind loads on the traffic light support structure. For this reason, a time-dependent approach by implementing the LES scheme was used in the CFD software ANSYS FLUENT. In the following, the formulations governed on the LES approach are further discussed.

LES was first developed based on the paper published by Smagorinsky [47]. LES filters the Navier-Stokes equations over a finite spatial region, and the purpose is to only explicitly solve the portions of turbulence greater than the filter width. The Navier-Stokes equations for the continuity and the incompressible flow without the body forces are [48]:

$$\frac{\partial u_i}{\partial t} + \frac{\partial u_i u_j}{\partial x_j} = -\frac{1}{\rho} \frac{\partial p}{\partial x_i} + \frac{\partial}{\partial x_j} \left(\nu \frac{\partial u_i}{\partial x_j} \right) \quad (13)$$

$$\frac{\partial u_i}{\partial x_j} = 0 \quad (14)$$

where, u_i , p , ρ stand for the velocity, pressure, and the density. The filter is a function of grid size. The approach is then a direct numerical solution by the filtered transient N-S equation. Eddies smaller than the filter width are removed and implicitly modeled based on a sub-grid scale (SGS) model which is a simple Eddy Viscosity model. The instantaneous component of the velocity, $u_i(x,t)$, is separated in a resolved part, $\bar{u}_i(x,t)$, and an unresolved part in a sub-grid scale, $u_i'(x,t)$.

$$u_i(x,t) = \bar{u}_i(x,t) + u_i'(x,t) \quad (15)$$

The filtered version of Navier-Stokes equation is:

$$\frac{\partial \bar{u}_i}{\partial t} + \frac{\partial(\bar{u}_i \bar{u}_j)}{\partial x_j} = -\frac{1}{\rho} \frac{\partial \bar{p}}{\partial x_i} + \frac{\partial}{\partial x_j} \left(\nu \frac{\partial \bar{u}_i}{\partial x_j} \right) - \frac{\partial \tau_{ij}}{\partial x_j} \quad (16)$$

where, τ_{ij} represents the sub-grid scale (SGS) Reynolds stress as following:

$$\tau_{ij} = \rho(\overline{u_i u_j} - \bar{u}_i \bar{u}_j) \quad (17)$$

The filtering operation is defined as:

$$\bar{\phi}(x) = \int_D \phi(x') G(x, x'; \bar{\Delta}) dx' \quad (18)$$

where, D is the entire fluid domain, and G is the filter function that defines the scale of the resolved eddies, and $\bar{\Delta}$ is the filter width. Three most widely used functions can be mentioned as, the Gaussian filter:

$$G(x-r) = \left(\frac{6}{\pi \bar{\Delta}^2} \right)^{0.5} \exp \left(-\frac{6(x-r)^2}{\bar{\Delta}^2} \right) \quad (19)$$

the sharp Fourier cutoff filter,

$$\hat{G}(k) = \begin{cases} 1 & \text{if } k \leq \pi \sqrt{\bar{\Delta}} \\ 0 & \text{otherwise} \end{cases} \quad (20)$$

and the top-hat filter in real space:

$$G(x-r) = \begin{cases} \frac{1}{\bar{\Delta}} & \text{if } |x-r| \leq \frac{\bar{\Delta}}{2} \\ 0 & \text{otherwise} \end{cases} \quad (21)$$

As mentioned before, in this study in order to capture the unsteady flow patterns around the traffic support structure, and then simulating the time history of wind-induced forces for the fatigue analysis, the LES scheme was used within the CFD software ANSYS FLUENT. In the solution method's box, SIMPLE scheme was selected for the pressure-velocity coupling, and a second order implicit scheme was imposed for the transient formulation with a time step of 0.01 s, and maximum 20 iterations in each time step. The time step was selected in a way that the Courant number to be less than 0.8. The dimensionless Courant number is defined as the following expression:

$$C = \frac{u\Delta t}{\Delta x} \quad (22)$$

where, u is the magnitude of the velocity, Δt is the time step, and the Δx stands for the mesh size.

Input Wind Velocity Profile

As described earlier, a UDF was written to introduce the transient inflow wind which accounts for the logarithmic velocity profile, and also the turbulence parameters. As a widely used approach, the variation of the mean wind velocity with height in the surface boundary layer can be simulated by using either logarithmic velocity profile or power-law velocity profile. In this study, the logarithmic velocity profile is introduced in the input UDF in order to simulate the transient inflow wind. Within the flat terrains, the logarithmic wind profile yields a good estimation for the vertical wind profile. The logarithmic wind velocity profile can be defined as [49]:

$$\bar{U}(y) = \frac{u_*}{k} \log_e \left(\frac{y}{y_0} \right) \quad (23)$$

where u_* is the friction velocity, k is known as von Karman's constant, and y_0 stands for the roughness length. Since the logarithmic of negative numbers do not exist, it is not applicable to use the logarithmic wind profile for the heights, y , below the zero-plane. To satisfy this condition, the domain was translated to the positive coordinates after importing the mesh file into the FLUENT. Due to similar mathematical difficulties in using the logarithmic wind velocity profile, wind engineers sometimes prefer to implement the power law expression for the wind velocity profile. The power law is defined as [49]:

$$\bar{U}(y) = \bar{U}_{10} \left(\frac{y}{10} \right)^\alpha \quad (24)$$

The aforementioned expression relates the mean wind speed at any height, y , with that at 10 m, \bar{U}_{10} . The exponent, α , depends on terrain roughness length and height ranges. It can be related as follows:

$$\alpha = \left(\frac{1}{\log_e(y_{ref}/y_0)} \right) \quad (25)$$

y_{ref} is the reference height which in this study the middle line of cantilevered arm was selected as the reference height ($y_{ref} = 5.3$ m).

Figure 45 shows the simulated CFD wind speed profiles compared with the input logarithmic velocity profile, and the log-law profile. From Figure 45, it can be seen that the two formulations are extremely close, and after the height above the reference point, the two wind velocity profiles are almost matched. But in the lower heights than the reference height, the log law expression results higher wind velocity. Both procedures are quite satisfying for engineering purposes [49]. Also, the mean velocity profile resulted from the CFD simulation is well matched with the input logarithmic velocity profile, meaning that the simulation has well progressed based on the anticipation, and properly mimics the wanted scenario for the input wind profile.

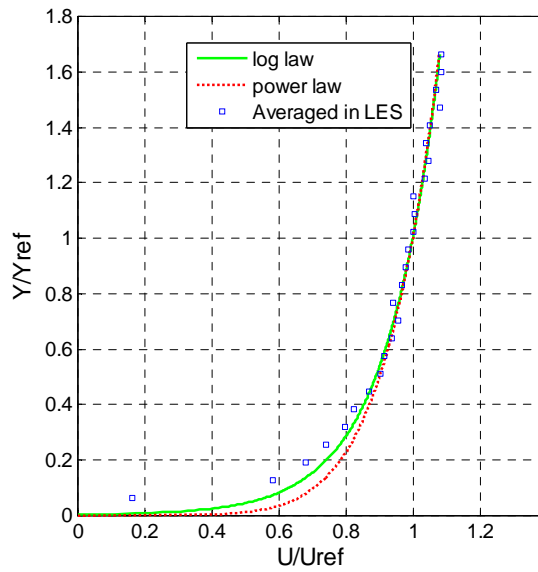


Figure 45
Simulated inlet wind speed profile

Drag and Lift Calculations

The time history of pressure values on the surface of the cantilevered arm are obtained by defining 8 monitoring rings on the length of the arm. Each ring captures the non-dimensional pressure coefficient, C_p , during the simulation at 8 monitoring points as are shown in the Figure 46. The equation (26) is used to define the non-dimensional pressure coefficient, C_p :

$$C_p(t) = \frac{p(t) - \bar{p}_s}{(1/2)\rho U^2} \quad (26)$$

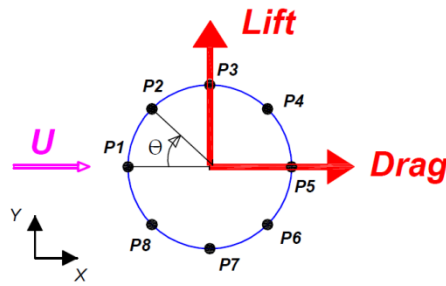
where, ρ is the air density, and the U stands for the mean wind speed measured at the reference height, i.e., the mean height of the cantilevered arm (5.4 m). The term of $p(t) - \bar{p}_s$

defines the difference of instantaneous pressure with respect to the mean static pressure. Afterwards, the drag and lift are calculated by integrating the surface pressure in each ring, and then extended to the whole arm length.

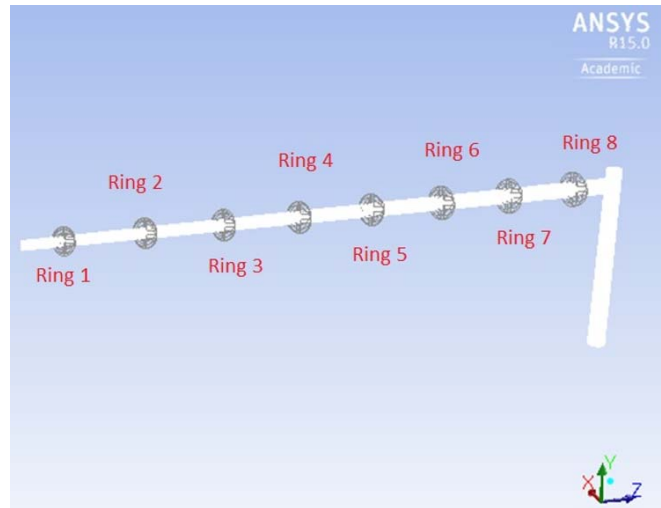
$$C_D(t) = \frac{1}{2} \int_0^{2\pi} C_p(t) \cdot \cos(\theta) d\theta = \frac{1}{2} \sum_i C_{p_i}(t) \cdot \cos(\theta_i) \Delta\theta_i \quad (27)$$

$$C_L(t) = \frac{1}{2} \int_0^{2\pi} C_p(t) \cdot \sin(\theta) d\theta = \frac{1}{2} \sum_i C_{p_i}(t) \cdot \sin(\theta_i) \Delta\theta_i \quad (28)$$

As can be seen in the Figure 46, θ is the angle between the defined points on the ring and the wind velocity direction.



A typical monitoring ring



A view of the rings defined on the mast arm

Figure 46

Points defined on the arm surface to measure the pressure coefficient

Finally, the lift and drag forces are calculated according to the following equation:

$$F = C_f \cdot q \cdot A \quad (29)$$

where, C_f stands for the drag and lift forces coefficients, q is the dynamics pressure which can be defined as $(1/2)\rho U^2$, and A is the area on the arm that is covered by each single monitoring points.

3-D Wind Model Results

Residuals, In CFD simulations a converged solution means that the results produced by the software are accurate enough, and matched to the physical aspects of the problem based on

the boundary conditions that are defined in the beginning of the simulation. As a general rule, a 3-5 orders of magnitude of convergence is an accepted range for most of the problems. Sometimes, the iterations may not yield very low residuals, but the values are not changing significantly while advancing the iterations. In this case, we may accept the results as a converged solution. If the solutions are not converged, one needs to keep the simulations running, until there is no big change in the residuals.

As explained earlier, LES is a transient simulation in which the flow field changes over the time; as a result, the residuals are expected to fluctuate with advancing the simulation, decreasing during the inner iterations and rising again once a new time step is started. In the 3-D CFD model, as an input value, 20 inner iterations are carried out within each time step to advance the simulation. Based on this definition, the simulations were performed within 499950 iterations, yielding the results of flow in 250 seconds of real time. The simulation would take a very long time if using personal computers. To alleviate this issue, High Performance Computing (HPC) resources were employed to run the model on parallel computing cores. With a rule of thumb, a supercomputer could be defined to be at least 100 times as powerful as a PC [50]. To run the CFD model in this study, 8 jobs were submitted on the LSU HPC, Philip clusters, with 1 node, 8 processors, and 48 GB memory per node, which took 384 hours running time.

Transient Inflow Wind Spectrum and Turbulence Intensity

According to the earlier sections, the logarithmic velocity profile is introduced in the input UDF in order to simulate the transient inflow wind. To verify the characteristics of the input wind velocity profile, monitoring points are defined in the inlet of the model. Figure 47 shows the time history of wind velocity in X-direction at reference height during the simulation time. It is seen that the velocity is fluctuating during the simulation time, developing the desired turbulence characteristic for the transient LES analysis.

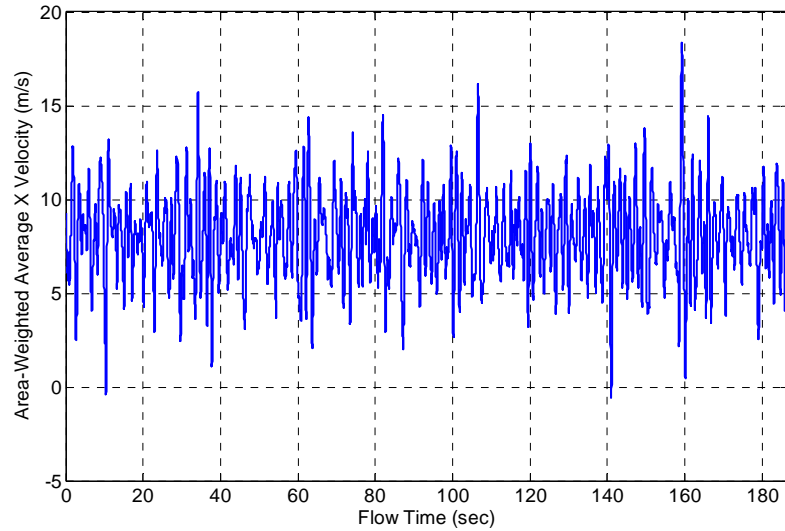


Figure 47
Time history of wind velocity in X- direction at reference height

The turbulence intensity is shown in the Figure 48 (a). As it is seen, the model simulated greater values for the turbulence intensity which is a strength point of the model, and is in favor of us. The normalized CFD wind velocity spectra along with the von Karman spectrum with the formulation taken from the Holmes, and the Kaimal spectrum taken from the Simiu are shown in the Figure 48 (b) [49, 51].

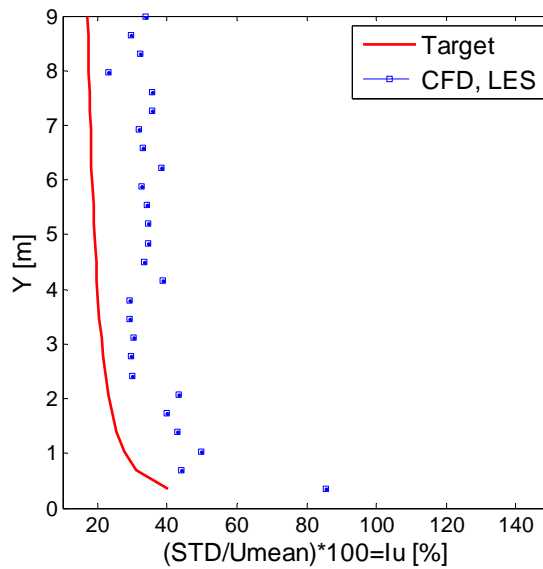


Figure 48
Results of input wind velocity profile

It can be seen that there are differences between the normalized CFD wind velocity spectra and the two aforementioned spectrums. It is aimed for future research to implement an

artificially wind velocity input that could best match with the defined target spectrums in order to mimic the distribution of energy in different frequencies similar to the target spectrums. Therefore, a new modified input UDF will be created and imposed to the computational model.

Dimensionless Pressure Coefficients (C_p)

As explained in earlier sections, in order to simulate the time history of wind forces on the support structures to be used for fatigue analysis, instantaneous pressure values are captured and monitored during the CFD simulation by defining monitoring points within the defined rings on the mast arm length. Figure 49 represents the mean value of the time series of non-dimensional pressure distributions within the 3 sections, rings of 1, 4, and 8 as are defined in Figure 46. It is worth noting that in this study, because the focus is not on the fluid-structure interactions, the structure is considered as a rigid body for the aerodynamic simulations.

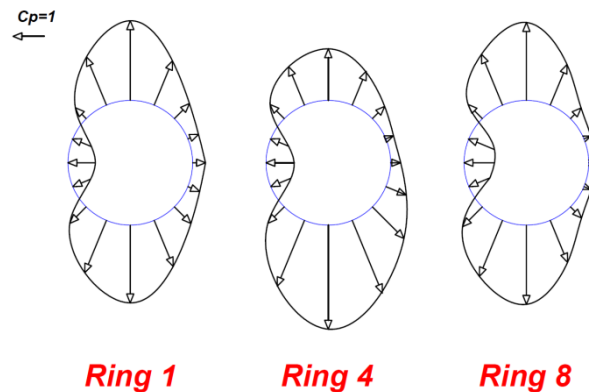


Figure 49
Mean value of time series of area-weighted averaged pressure coefficient
within the monitoring points

From Figure 49 it is seen that the pressure distributions have a symmetric pattern about the x-axis (the line from $\theta = 0$ to $\theta = 180$ degrees), which means that the lift forces which are a resultant of the difference of pressure distributions on the upper and the lower sides of the cylinder may be in a lower range in compare to the drag forces. Although the value of the lift force is important, the time variation of the lift forces are much more crucial in the fatigue analysis of the support structure which are achievable from the simulation. In contrast to the pressure distributions on the above and lower sides, the pressure distributions in front and the aft of the cylinder are not symmetric, so the calculation may yield bigger drag forces in compare to the lift forces. This fact is examined within the next section. Figure 50 depicts distribution of mean pressure coefficient around the cylinder for 2 cases of 3-D LES CFD model, and experimental results.

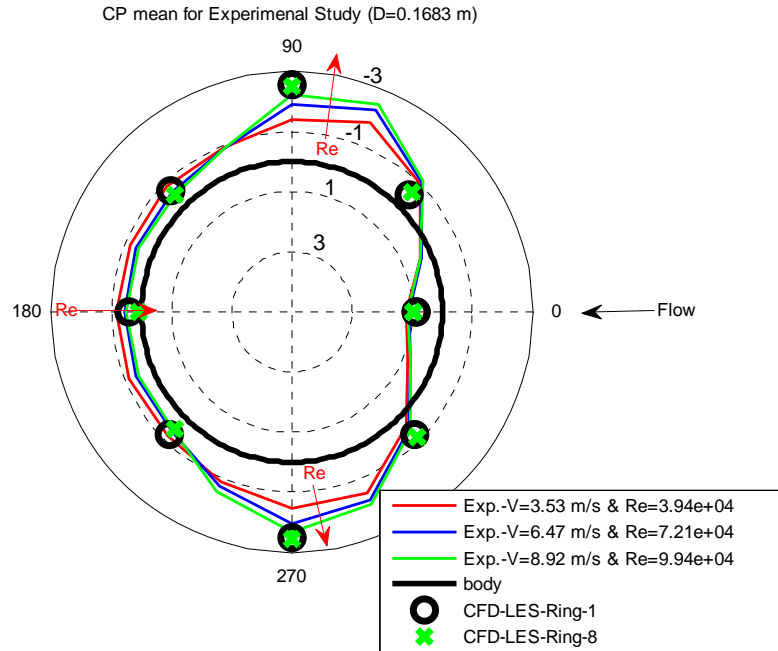
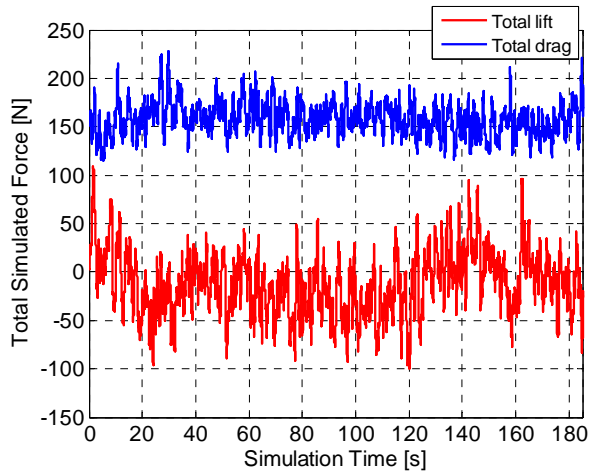


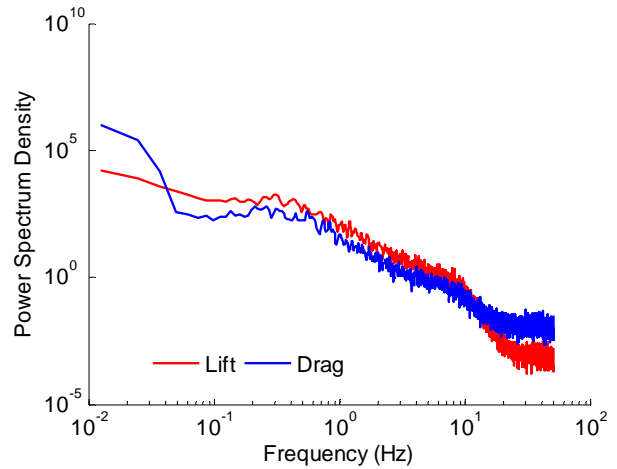
Figure 50
Distribution of mean pressure coefficient around the cylinder for 2 cases

Final Simulated Drag and Lift Forces

The total simulated lift and drag forces exerted on the body of cantilevered arm are plotted in Figure 51 (a). It is seen that the time history of forces yield a greater value for the drag forces. This fact could be predicted by looking at Figure 49, and the mean value of time series of average of pressure coefficients. The lift force is fluctuating in a greater range, resulting a standard deviation twice of the values of standard deviation for the drag forces. This fluctuation over the simulation time is an interesting result for the fatigue analysis of the support structures. In Figure 51 (b), the power spectrum density of lift and drag forces are represented. It is seen that the lift produces more energy within the lower frequencies which are dominated in wind-induced loads.



a. Power Spectrum Density for Drag forces on Section 4



b. Power Spectrum Density for Lift forces on Section 4

Figure 51

Lift with standard deviation of $\text{std} = 32.38$ [N], and drag with $\text{std} = 16.99$ [N]

Finally, the time series of simulated wind-induced loads on the structure which are monitored at 8 rings through the length of the mast arm length are plotted in Figure 52. These simulated loads from the CFD model were extracted and imposed on dynamic model in SOLIDWORKS.

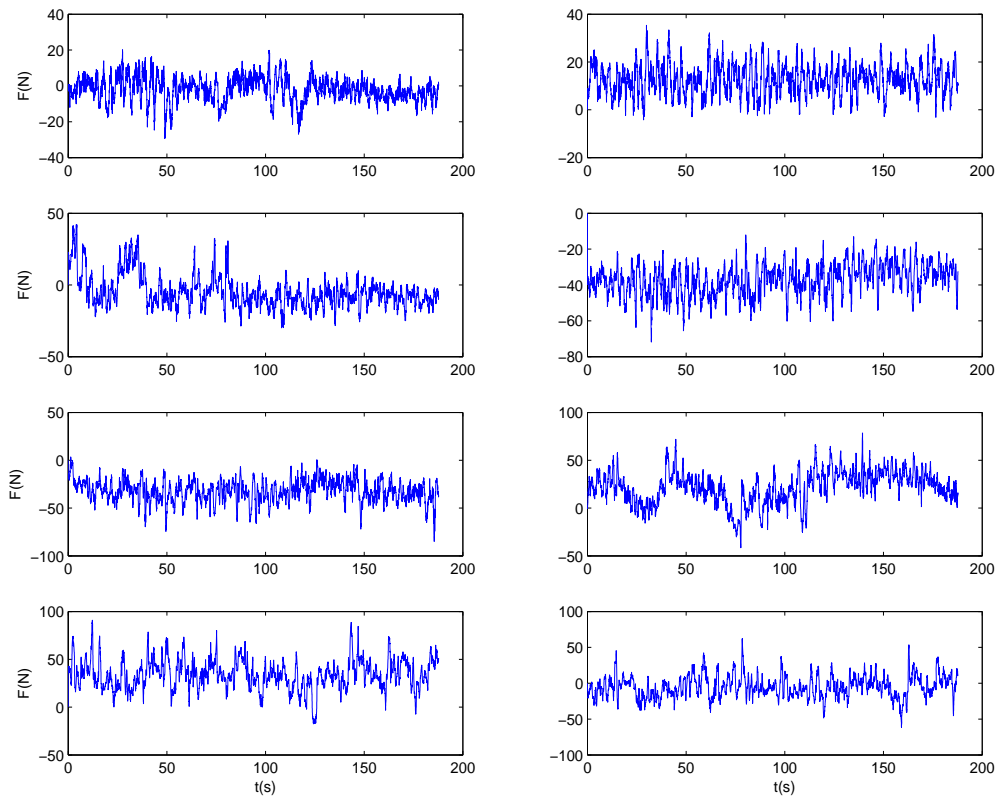


Figure 52
Time series of wind-induced loads on the different parts of the mast arm

Vibration Mitigation

The methodology that was used for dynamic study and vibration control is illustrated in Figure 53. The parts in blue are the dynamic model related steps and ones in green are related to the CFD model. At the first step it is necessary to define the physical properties of the structure in the structural models. In this study, both the SOLIDWORKS finite element method and a lumped mass method developed in the MATLAB were implemented. According to the physical properties of the structure, a CFD model is used to extract the loads on the structure and the results were imported in the models as excitation loads. To control the structure, a single degree of freedom (SDOF) system is modeled and the dampers' properties are optimized.

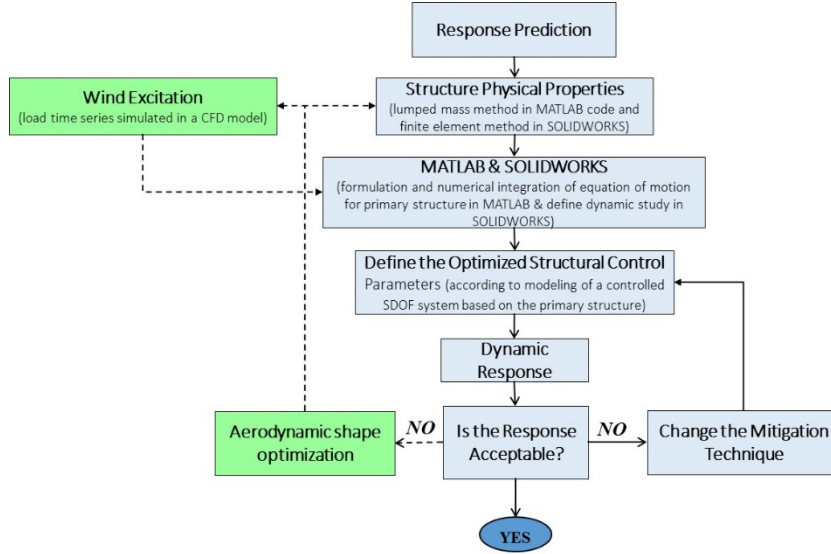


Figure 53
Methodology were used for the dynamic study

Equation of Motion for the Multi-Degree Freedom System

In the first step to study a control problem, there is a need to obtain the equations of motion for the structure and model the system. According to Newton's second law, the equation of motion for a multi-degree of freedom system can be written as follows:

$$\mathbf{M}\ddot{\mathbf{X}}(t) + \mathbf{C}\dot{\mathbf{X}}(t) + \mathbf{K}\mathbf{X}(t) = \Lambda\mathbf{P}(t) + \mathbf{\Gamma}\mathbf{f}(t) \quad (30)$$

where, \mathbf{M} , \mathbf{C} , and \mathbf{K} are the mass, damping and stiffness matrices relatively. Λ is a vector of ones, \mathbf{P} is the external excited force, $\mathbf{\Gamma}$ is a matrix representing position of control forcing and \mathbf{f} is a vector of control forces. In state space representation, the dynamic system can be written as a first order vector-matrix differential equation as follows:

$$\dot{\mathbf{z}} = \mathbf{A}\mathbf{z} + \mathbf{B}\mathbf{f} + \mathbf{E}\mathbf{P} \quad (31)$$

$$\mathbf{y} = \mathbf{C}\mathbf{z} + \mathbf{D}\mathbf{f} \quad (32)$$

$$\mathbf{A} = \begin{bmatrix} \mathbf{0}_{n \times n} & \mathbf{I}_{n \times n} \\ -\mathbf{M}^{-1}\mathbf{K} & -\mathbf{M}^{-1}\mathbf{C} \end{bmatrix}, \quad \mathbf{B} = \begin{bmatrix} \mathbf{0}_{1 \times n} \\ \mathbf{M}^{-1}\mathbf{\Gamma} \end{bmatrix}, \quad (33)$$

$$\mathbf{C} = \begin{bmatrix} \mathbf{M}^{-1}\mathbf{K}\mathbf{M}^{-1}\mathbf{C} \\ \mathbf{I}_{n \times n} & \mathbf{0}_{n \times n} \\ \mathbf{0}_{n \times n} & \mathbf{I}_{n \times n} \end{bmatrix}, \quad \mathbf{D} = \begin{bmatrix} \mathbf{M}^{-1}\mathbf{\Gamma} \\ \mathbf{0}_{2n \times n} \end{bmatrix}, \quad (34)$$

$$\mathbf{E} = \begin{bmatrix} \mathbf{0}_{1n \times n} \\ \mathbf{\Lambda} \end{bmatrix} \quad (35)$$

here, A is called the state matrix, B is input matrix, C the output matrix, and D the direct transformation matrix.

Generation of the Mass, Stiffness and Damping Matrices

For control purposes in this study, a lumped mass model is derived. In this model, the mass of the building is lumped at the positions of mast arm. The positions of concentrated masses are shown in Figure 54. The lumped mass matrix is as follows. It is an orthogonal matrix with the masses at the orthogonal and zero at other arrays.

$$\mathbf{M} = \begin{bmatrix} M_1 & 0 & \dots & 0 \\ 0 & M_2 & \dots & 0 \\ \dots & \dots & \dots & \dots \\ 0 & 0 & \dots & M_8 \end{bmatrix} \quad (36)$$

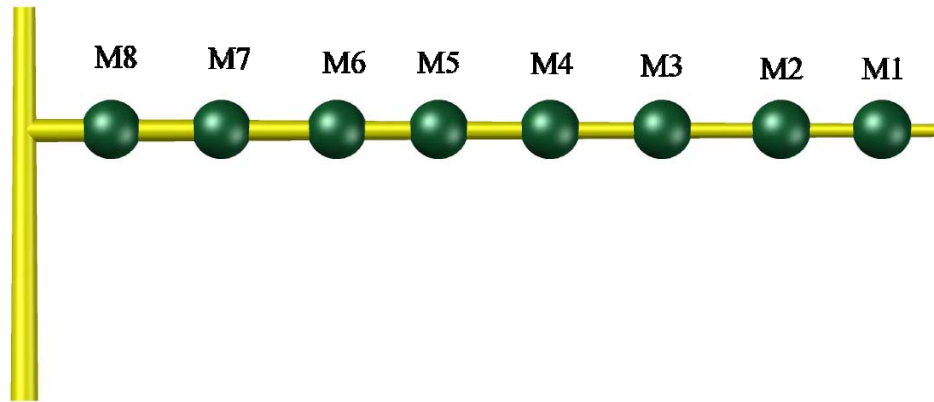


Figure 54
Concentrated masses through the mast arm

The stiffness matrix was obtained using the flexibility matrix. In this regard, the virtual work method is used to define the deflection of a unit load at different positions through the mast arm:

$$\delta_{ij} = \int_0^a \frac{M_i(x)m_j(x)}{EI(x)} dx \quad (37)$$

where, δ_{ij} is the displacement of point j when the load is at point i and $M(x)$ is the real load and $m(x)$ is the virtual work. Since the mast arm is tapered, the moment of inertia of the mast

arm is a function of x. Therefore, the Gaussian Quadrature method is used to solve the integration according to the following equation:

$$\int_a^b f(x)dx = \frac{b-a}{2} \sum_{i=1}^n w_i f\left(\frac{b-a}{2}x_i + \frac{a+b}{2}\right) \quad (38)$$

where, w_i are Gaussian weights and x_i are Gaussian points.

$$\mathbf{S} = \begin{bmatrix} \delta_{11} & \delta_{12} & \dots & \delta_{18} \\ \delta_{21} & \delta_{22} & \dots & \delta_{28} \\ \dots & \dots & \dots & \dots \\ \delta_{81} & \delta_{82} & \dots & \delta_{88} \end{bmatrix} \quad (39)$$

\mathbf{S} is the flexibility matrix. To obtain the stiffness matrix, an inverse has to be made as follows: $\mathbf{K} = \text{inv}(\mathbf{S})$. Using eigenvalue problem, the natural frequencies of the structure will be accessible and then the damping matrix is obtained using Rayleigh damping which is proportional to the mass and stiffness matrices as follows:

$$\mathbf{C} = \alpha\mathbf{M} + \beta\mathbf{K} \quad (40)$$

here α and β are predefined constants. After calculating the damping matrix, the modal damping vector is estimated for all the vibrational modes and the damping ratios are replaced by 1%. The damping matrix is reconstructed using the new modal damping vector [43].

Tuned Mass Damper

In order to reduce the signal support structures' vibration-induced displacements, using a tuned mass damper is conventional and, based on the literature, is an effective method. Mass spring system with oil damper install on the vibrating primary structure at anti-node position to reduce vibrations [52]. Principally the tuning mass is usually about 2% of the primary structure and is tuned to a particular structural frequency, so that when that frequency is excited, the damper will suppress the vibration by its out of phase motion. For a SDOF system controlled by a tuned mass damper, the equations of motion can be written as follows: primary structure:

$$(1+\bar{m})\ddot{U} + 2\xi\omega\dot{U} + \omega^2U = \frac{P}{M} - \bar{m}\ddot{u} \quad (41)$$

damper:

$$\ddot{u} + 2\xi_d\omega_d\dot{u} + \omega_d^2u = -\ddot{U} \quad (42)$$

Here, $\bar{m} = m/M$ and M and m are the masses of the primary structure and the damper, respectively. Also

$$\omega^2 = \frac{K}{M} \quad (43)$$

$$C = 2\xi\omega M \quad (44)$$

K is the structure's stiffness, ξ is the damping ratio, U is the structure's displacement, and u is the displacement of the damper. Common design parameters for TMDs are the mass, the stiffness, and the damping ratio of the auxiliary system. According to Warburton and Ayorinde, the primary structure can be treated as an equivalent SDOF system if its natural frequencies are well separated [53]. Then the effect of the TMD can be viewed as being equivalent to changing the damping ratio of the original system from the value $\xi = C/2(KM)^{0.5}$ to a larger value ξ_e [54]. The equivalent system has the same mass and stiffness as the primary structure but with damping $C_e = 2\xi_e(KM)^{0.5}$. Then it can be shown that [55]:

$$\xi_e = \frac{1}{2} \frac{\alpha_1(\alpha_2\alpha_3 - \alpha_1) - \alpha_0\alpha_3^2}{\alpha_0(\alpha_2\alpha_3 - \alpha_1) + \alpha_3(\beta_1^2 - 2\alpha_0) + \alpha_1} \quad (45)$$

$$\begin{aligned} \alpha_0 &= f^2, \quad \alpha_1 = 2f(\xi f + \xi_d), \quad \alpha_2 = 1 + f^2(1 + \mu) + 4f\xi\xi_d \\ \alpha_3 &= 2\xi + 2\xi_d f(1 + \mu), \quad \beta_1 = 2\xi_d f \end{aligned} \quad (46)$$

where, $\mu = m/M$, $f = \omega_d / \omega$

Feng and Mita proposed formulae for estimating the optimum parameters of the TMD by minimizing the mean square response of the primary structure to a white-noise force excitation for wind analysis [56]. For wind loading, they proposed the following absorber parameters:

$$f = \frac{\sqrt{1 + (\mu/2)}}{1 + \mu}, \quad \xi_d^{opt} = \frac{1}{2} \sqrt{(1 + \mu)f^4 - \left(\frac{2 + \mu}{1 + \mu}\right)f^2 + \frac{1}{1 - \mu}} \quad (47)$$

In order to find the TMD control parameters, a SDOF system with a damping ratio of 2% was modelled. The system was loaded by a with-noise excitation and various parameters controlled. Figure 55 shows the normalized displacement response of a SDOF system controlled by a TMD with a 2% mass ratio. The figure depicts that the optimum values of the tuning frequency ratio and the damping factor for the TMD are 0.925 and 0.09, respectively and the TMD is able to reduce the STD of the displacement response by 38%. In Figure 56 the equivalent damping ratio of the system by changing the mass ratio is shown. All of the TMD parameters, then can be obtained using these two graphs. According to Figure 56, if a

TMD with a mass ratio of 2% (i.e., the TMD mass is equal to 2% of primary structure) is used then the equivalent damping ratio of whole the system will increased up to about 4.3%.

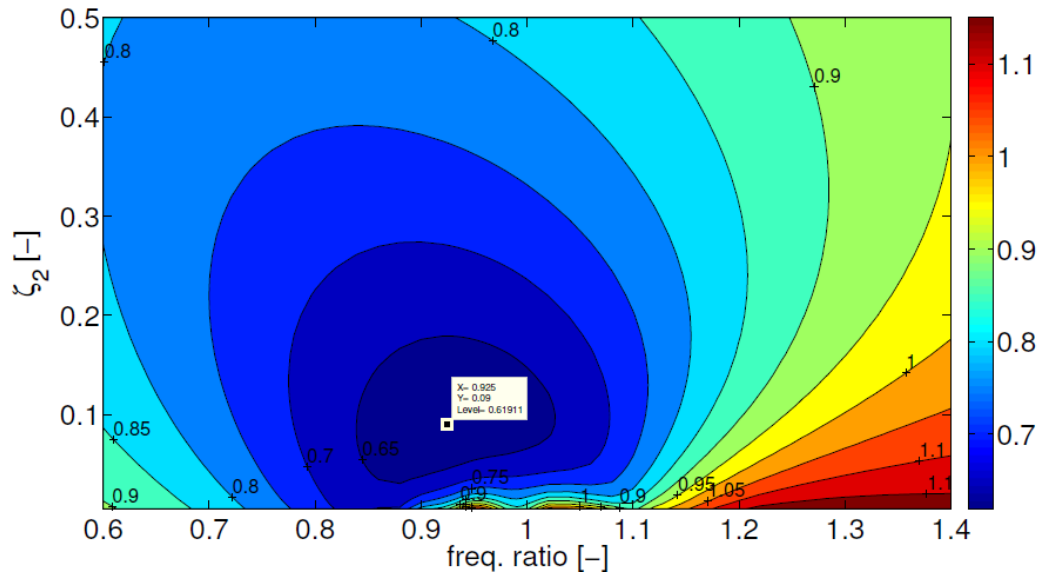


Figure 55
Changing the frequency and damping ratios of the TMD

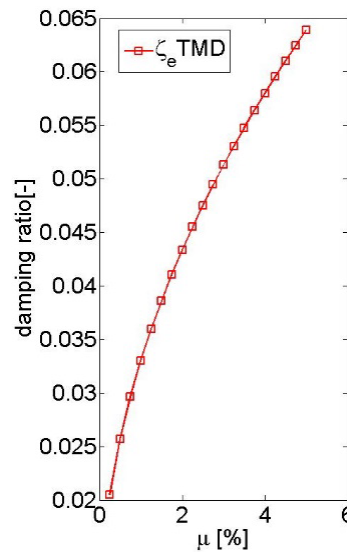


Figure 56
Equivalent system damping ratio for different mass ratios

Dynamic Study

In order to evaluate the performance of using tuned mass dampers to suppress the vibration of cantilevered signal support structures, numerical model tests are conducted in SOLIDWORKS. Here, the tapered mast arm and the pole are the same as the wind model and have the same length as the structure that are used in the experimental study of Christenson et

al. [35] (Figure 57). A frequency analysis study is done and the first four modal shapes are shown in Figure 58 (top left: 1st out-of-plane, top right: 2nd out-of-plane, bottom left: 1st in-plane, bottom right: 2nd in-plane). In Figure 59 the in-plane modal shape of the mast arm is plotted for both lumped mass and SOLIDWORKS models. According to the analysis, the fundamental in-plane frequency is 0.9 Hz and the first out-of-plane frequency is 0.75 Hz. Figure 60 shows the displacement of the free-end of the mast arm with and without the dampers. According to the results, the vibration of the structure with 3 tuned mass dampers is reduced up to 37%. In Figure 61 the stress at fixed-end point of the mast arm is plotted for both controlled and uncontrolled structure. Here, the stress is reduced up to 53% by controlling the vibration of the structure.

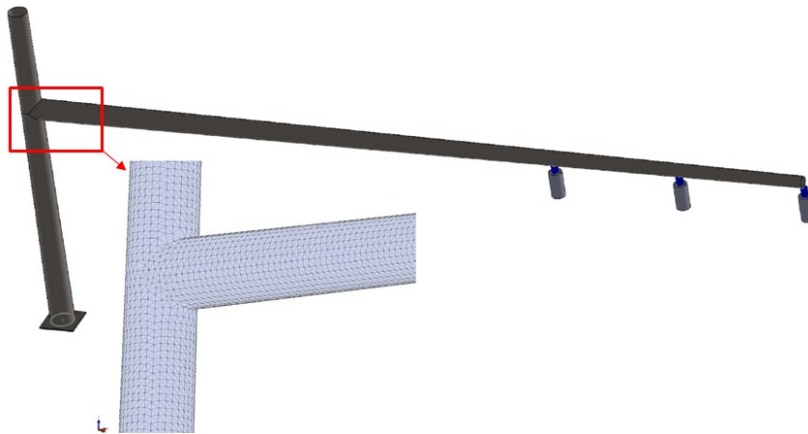


Figure 57
Cantilevered signal support structure used for simulation

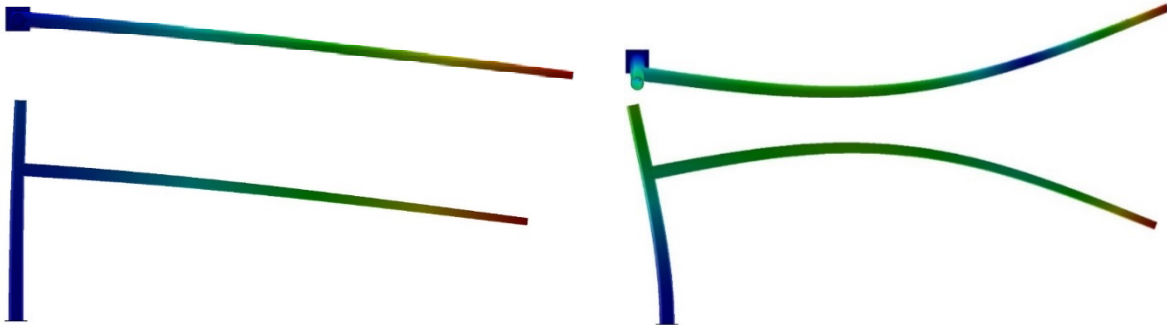


Figure 58
Modal shapes of the cantilevered support structure

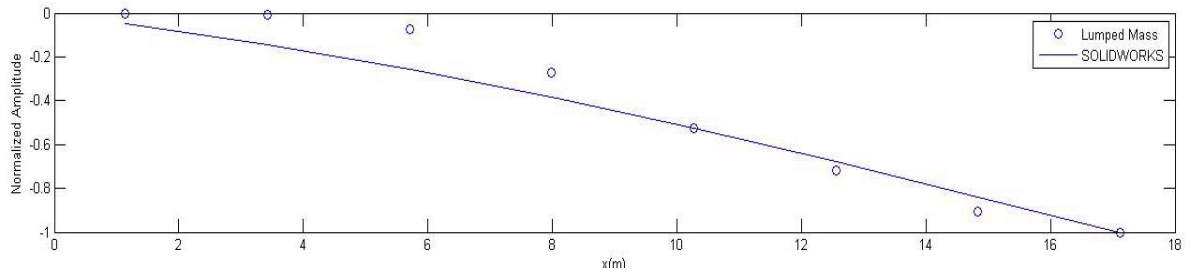


Figure 59
Modal shapes of the cantilevered support structure

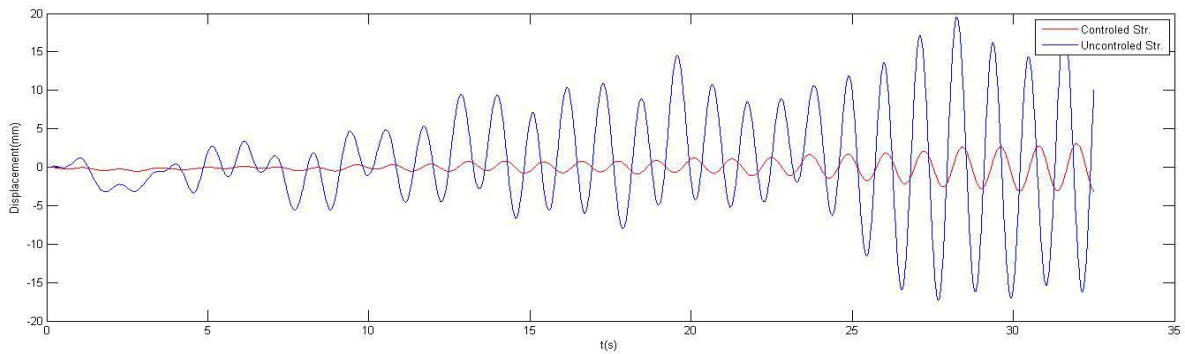


Figure 60
Displacement of the mast arm free-end for controlled and uncontrolled structure

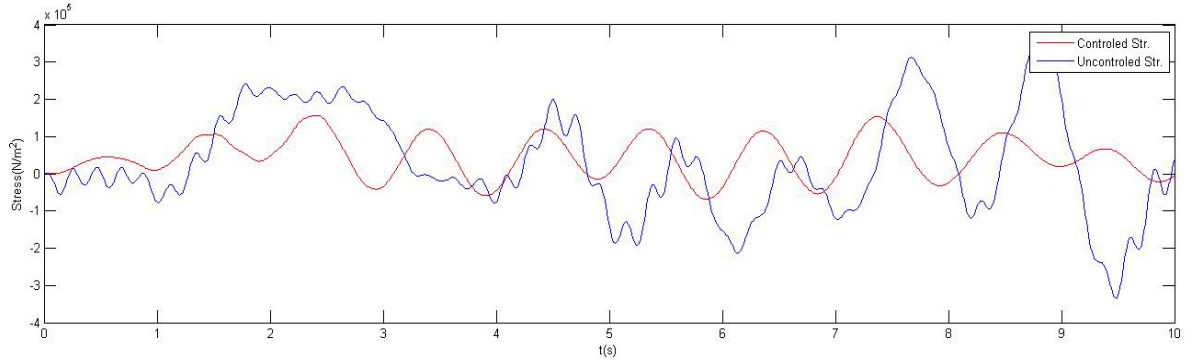


Figure 61
Stress at the mast arm fixed-end for controlled and uncontrolled structure

DISCUSSION OF RESULTS

This report presented a methodology to suppress wind-induced vibrations in a mast arm cantilever traffic signal support structure with a circular cylinder section by using the CFD simulations, experimental validation, and a dynamic model with external dampers. The aerodynamic characteristics of the structure were investigated by employing a transient RSM 2-D CFD model, which was validated by experimental testing that took place at the open-jet facility at LSU. After ensuring that the CFD model was able to simulate flow patterns, and vortex shedding effects for this type of structure were properly captured, a more elaborate 3-D CFD model was implemented by using a time-dependent approach LES scheme. The model was run on LSU HPC clusters. Monitoring points were defined on the mast arm to capture the pressure coefficients, and then to calculate lift and drag forces on the body.

It was concluded that the CFD model yields acceptable results for the pressure distribution around the body based on the comparison with the experimental results. In addition, the time histories of wind-induced loads have indicated that the simulated lift forces are fluctuating in greater ranges, resulting in a standard deviation twice of the value of the standard deviation for the drag forces. Appropriately capturing this fluctuation trend over the simulation time is an interesting result for the fatigue analysis of the support structure.

The simulated wind-induced loads were then used in a dynamic model to evaluate the influence of three dampers to reduce the vibration and stresses in the system. In order to mitigate the vibrations, tuned mass dampers are proposed. The structural response with and without the dampers were simulated in a dynamic model. Also in order to optimize tuned mass dampers' parameters, a SDOF system was modeled, and different parameters were compared and finally dampers with a mass ratio of 2% were selected.

In order to mitigate the vibrations, distributed tuned mass dampers were investigated, making use of the available weights of the lighting boxes. The structural response with and without the dampers were simulated by a dynamic model. The dynamic analysis showed that damping enhancement in traffic lighting structures can significantly reduce vibration-induced stress, with promises to improve the safety to the traveling public, extend the life of existing traffic structures, increase traffic efficiency, and reduce the cost of new structures. Moreover, the generated wind load time histories with the dynamic model are being used for different vibration control schemes, including passive and semi-active control devices with drift magnification connections, with the objective of building a database useful for creating

guidelines and recommendations on the proper use of damping enhancement devices, for future implementation in the AASHTO standard.

CONCLUSIONS

Cantilevered signal support structures are the most common type of structures for traffic signals. These very flexible structures are considered slender and lightly damped structures with large vibration amplitude when subjected to wind loads. According to the literature, fatigue failure due to wind-induced vibrations is very common. To help investigate potential solutions to wind-induced vibrations in traffic lightening structures, the current study evaluated the aerodynamic loads of a mast arm cantilever traffic signal support structure by employing CFD simulations using a time dependent approach LES. The CFD results were validated by experimental testing on a section model of the mast arm. The simulated wind-induced loads were then used in a dynamic model in to evaluate the influence of three dampers to reduce the vibration and stresses in the system. The main contributions of the current study can be summarized as follows:

- The CFD and experimental tests gave comparable results that reveal the capabilities of the CFD to capture wind loads on traffic light support structures.
- The methodology presented in this paper was successful producing time histories of wind-induced forces which are required to simulate the dynamic responses of the structure. Although the LES scheme has yielded reasonable results, it still needs considerable computational efforts which can be a subject of further investigations.
- Results have indicated that the simulated lift forces have a standard deviation of two times the value for the drag forces. These fluctuations over the simulation time is an interesting result for the fatigue analysis of the support structures.
- The simulation results revealed that the dampers can effectively control the vibration of the structure and can reduce the displacements of the free end of the mast arm up to 37%. Also, the dampers can reduce the stress at the fixed end of the mast arm up to 53%. The reduction of the displacement and stresses show promise for improving the safety of the traveling public, extend the life of existing traffic structures, increase traffic efficiency, and reduce the cost of new structures.
- The generated wind load time histories with the dynamic model will be used for different vibration control schemes, including passive and semi-active control devices with drift magnification connections, with the objective of building a database useful for creating guidelines and recommendations on the proper use of damping enhancement devices, useful for implementation in the AASHTO standard.

RECOMMENDATIONS

According to the simulation results, it is highly recommended to use tuned mass dampers (TMDs) in order to suppress and effectively control the vibration of the structure and reduce the displacements of the free end of the mast arm. Dampers also can help to reduce the stress at the fixed end of the mast arm. As a tangible result, the reduction of the displacement and stresses can increase the fatigue life of the structure.

It is recommended for future research studies, along with structural optimization, to examine aerodynamic shape optimization as an additional alternative to alleviate wind effects on the primary structure.

It is suggested to investigate the scale effects on the aerodynamic loads, both in CFD simulations and laboratory measurements.

It is recommended to conduct field study and wind load measurements in full-scale and open-terrain condition.

The generated wind load time histories with the dynamic model should be used for different vibration control schemes, including passive and semi-active control devices with drift magnification connections, with the objective of building a database useful for creating guidelines and recommendations on the proper use of damping enhancement devices, for future implementation in the AASHTO standard.

ACRONYMS, ABBREVIATIONS, AND SYMBOLS

AASHTO	American Association of State Highway and Transportation Officials
A	Fatigue detail constant
b	the flat-to-flat width of the member
cm	centimeter(s)
C	damping matrices
C_p	Non-dimensional pressure coefficient
C_l	Lift coefficient
C_d	Drag coefficient
C_f	Drag and lift forces coefficients
CFD	Computational fluid dynamic
D	Cross-wind dimension of element
DNS	Direct Numerical Simulation
DOTD	Louisiana Department of Transportation and Development
FHWA	Federal Highway Administration
ft.	Foot (feet)
f_n	the first natural frequency of the structure
f	vector of control forces
G	Filter function in LES formulations
HPC	High Performance Computing
in.	inch (es)
IF	importance factor
k	von Karman's constant
K	stiffness matrices
LTRC	Louisiana Transportation Research Center
LES	Large Eddy simulation
LSU	Louisiana State University
m	meter(s)
M	Mass matrices
N	Fatigue life
PG	Pressure developed by galloping effect
$p(t) - \bar{p}_s$	Instantaneous pressure with respect to mean static pressure
q	Dynamics pressure
RE	Reynolds number

RSM	Reynolds Stress Model
RANS	Reynolds-averaged Navier-Stokes
S	Strouhal number
SGS	sub-grid scale
SDOF	single degree of freedom
lb.	pound(s)
u	Upward velocity of body
u_*	Friction velocity
\overline{U}_{10}	Mean wind speed at any height of 10 meters
V	freestream wind velocity
V_m	yearly mean wind velocity
V	Truck velocity
y_0	Roughness length
y_{ref}	Reference height

Greek symbols

α	Downward angle of wind attack
β	damping ratio
τ_{ij}	Sub-grid scale (SGS) Reynolds stress
$\overline{\Delta}$	Filter width in LES formulation
Δx	Mesh size
Δt	Time step
ρ	Air density
Γ	Matrix representing position of control forcing

REFERENCES

1. Dexter, R. J. and Ricker, M. J. "Fatigue-Resistant Design of Cantilevered Signal, Sign, and Light Supports," Washington, D.C., University of Minnesota: 111, 2002.
2. Cruzado, H. "Risk Assessment Model for Wind-Induced Fatigue Failure of Cantilever Traffic Signal Structures," 2007.
3. Cook, R. A., Bloomquist, D., Kalajian, M. A., & Cannon, V. A. "Mechanical Damping Systems for Traffic Signal Mast Arms," *Engineering and Industrial Experiment Station*, University of Florida, 1998.
4. Kaczinski, M.R., Dexter, R.J., Dien, J.P.V., "Fatigue-Resistant Design of Cantilevered Signal, Sign and Light Supports," Washington, D.C.: *National Academy Press*, 1996.
5. Hartnagel, B.A., and Barker, M.G., "Strain measurements of traffic signal mast arms," *Structural Engineering in the 21st Century*, New Orleans, LA. USA, Reston, VA: American Society of Civil Engineers, 1999.
6. Chen, G., Wu, J., Yu, J., Dharani, L. R. and Barker, M. "Fatigue assessment of traffic signal mast arms based on field test data under natural wind gusts," *Transportation Research Record* 1770: 7, 2001.
7. Hart, J.D. "City Traffic Engineer of Lubbock," Texas. USA, 2005.
8. Letchford, C., and Cruzado, H., "Risk Assessment Model for Wind-Induced Fatigue Failure of Cantilever Traffic Signal Structures," *Texas Department of Transportation*, Texas Tech University, 2008.
9. McDonald, J. R., Mehta, K. C., Oler, W., & Pulipaka, N., "Wind Load Effects on Signals, Luminaires and Traffic Signal Structures," Lubbock, Texas: *Wind Engineering Research Center*, Texas Tech University, 1995.
10. CNN, <http://www.cnn.com/2015/04/09/us/severe-weather/>, page visited on April 9, 2015.
11. Christenson, R. "Reducing Fatigue in Wind-Excited Traffic Signal Support Structures using Smart Damping Technologies," USA, *University of Connecticut*, 2011.
12. Cook, R. A., Bloomquist, D., Richard, D. S. and Kalajian, M. A. "Damping of Cantilevered Traffic Signal Structures," *Structural Engineering* 127(12): 8, 2001.

13. Cook, R. A. and Bloomquist, D. "Design, testing and specification of a mechanical damping device for mast arm traffic signal structures," Florida, USA, *University of Florida*: 149, 2000.
14. Walshe, D. E., and Wootton, L. R., "Preventing Wind-Induced Oscillations of Structures," *Proceedings, Institute of Civil Engineers*, Vol. 47, pp. 1-24, 1970.
15. Kolousek, V., "Wind effects on civil engineering structures," New York, USA, *Elsevier*, 1984.
16. Zuo, D., and Letchford, C. W., "Wind-induced vibration of a traffic-signal-support structure with cantilevered tapered circular mast arm," *Engineering Structures* 32: 9, 2010.
17. Smith, J. W., "Vibrations of structures - Applications in civil engineering design," New York, *Chapman and Hall*, 1988.
18. Sachs, P., "Wind forces in Engineering," England, *Pergamon Press, Oxford*, 1978.
19. Hamilton, H. R., Riggs, G. S., & Puckett, J. A., "Increased Damping in Cantilevered Traffic Signal Structures." *Structural Engineering*, 2000.
20. Creamer, B. M., Frank. K. H. and Klingner. R. E. "Fatigue loading of cantilever sign structures from truck wind gusts," *Ctr. for Hwy. Res. USA, University of Texas*, Austin, 1979.
21. Cook, R. A., Bloomquist. D., Agosta. A. M. and Taylor. K. F. "Wind load data for variable message signs," Gainesville, FL, USA, *Engineering and Industrial Experiment Station University of Florida*, 1996.
22. Pulipaka, N., Sarkar, P. P., McDonald, J. R., "On galloping vibration of traffic signal structures," *Wind Engineering and Industrial Aerodynamics*, 77 & 78, 10, 1998.
23. Foley, C. M., Diekfuss, J. A., Wan., B. "Fatigue risks in the connections of sign support structures," Wisconsin, USA, *Marquette University*, 2013.
24. AASHTO Specifications: American Association of State Highway and Transportation Officials (2001). *Standard Specifications for Structural Support for Highway Signs, Luminaires, and Traffic Signals*. Washington, D.C. USA.
25. Diekfuss, J. A. "Reliability-based fatigue assessment of mast-arm sign support

- structures,” Milwaukee, WI, *Marquette University*. PhD, 2013.
26. Hamilton, H. R., Puckett, J. A., Gray, B., Wang, P., Deschamp, B., McManus, P., “Traffic Signal Pole Research,” Laramie, WY, *University of Wyoming*: 158, 2002.
 27. Richman, N. B., “Fatigue life investigation of high performance mast arm base plate connections,” Austin, TX. USA, *University of Texas at Austin. Master of Science*: 162, 2009.
 28. Frank, K. H., “Fatigue Strength of Signal Mast Arm Connections,” *University of Texas at Austin*, 2005.
 29. Jacobsen, J. J., “Traffic signal mast arm structural issues and investigations Florida. USA,” *Florida State University*, 2013.
 30. Repetto, M. P., and Solari. G., “Wind-induced fatigue collapse of real slender structures,” *Engineering Structures* 32: 11, 2010.
 31. <http://www.theguardian.com/world/2010/dec/10/new-orleans-police-convicted-katrina-killing>, Photograph: Robert Sullivan/AFP.
 32. <http://didierruef.photoshelter.com/image/I00008zws6ZzZTH0>.
 33. Medina, M. M., “Development of design specifications, details and design criteria for traffic light poles,” Lawrence, Kansas, USA, *University of Kansas*: 60, 2006.
 34. McManus, P. S., III, H. R. H., Puckett, J. A., “Damping in Cantilevered Traffic Signal Structures under Forced Vibration,” *Structural Engineering*, 129(3), 10, 2003.
 35. Christenson, R., Cashany, M., Hua, J., Zuo, D., “Field testing of signal head vibration absorber to reduce fatigue in wind-excited traffic signal support structures”, *Journal of Transportation Research Board, structures*, Volume 1, pp 42-48, 2014.
 36. Bursnall, W.J., and Loftin, L.K.J., “Experimental investigations of the pressure distribution about a yawed circular cylinder in the critical Reynolds number range,” *National Advisory Committee for Aeronautics*, 1951.
 37. Roshko, A., “Experiments on the row past a circular cylinder at very high Reynolds number,” *Journal of Fluid Mechanics*, Vol. 10, pp. 345-356, 1955.
 38. Achenbach, E., and Heinecke, E. “On Vortex Shedding from Smooth and Rough

- Cylinders in the Range of Reynolds Numbers 6×10^3 to 5×10^6 ,” *Journal of Fluid Mechanics*, Vol.109, pp. 239-251, 1981.
39. Raghavan, K., Bernitsas, M. M., “Experimental investigation of Reynolds number effect on vortex induced vibration of rigid circular cylinder on elastic supports,” *Ocean Engineering*, 38, pp. 719–731, 2011.
 40. Belloli, M., Giappino, S., Morganti, S., Muggiasca, S., Zasso, A., “Vortex induced vibrations at high Reynolds numbers on circular cylinders,” *Ocean Engineering*, Volume 94, 15 January, Pages 140-154, 2015.
 41. ANSYS FLUENT 12.0, Theory Guide, ANSYS Inc. April 2009.
 42. FLUENT. ANSYS FLUENT user’s guide. Canonsburg, PA 15317: ANSYS, Inc. Release 14.0, Southpointe, 275 Technology Drive, November 2011.
 43. Aly, A. M., “Proposed robust tuned mass damper for response mitigation in buildings exposed to multidirectional wind,” *The Structural Design of Tall and Special Buildings*, 23(9), 664-691, 2014.
 44. Scanivalve (Intelligent Pressure and Temperature Instrumentation), Webpage: <http://www.scanivalve.com>.
 45. ICEM CFD. User’s guide. Canonsburg, PA 15317: ANSYS Inc.; Release 14.0, Southpointe, 275 Technology Drive, 2011.
 46. Spalart, P., Deck, S., Shur, M., Squires, K., Strelets, M., Travin, A., “A new version of detached eddy simulation, resistant to ambiguous grid densities,” *Journal of Theoretical and Computational Fluid Dynamics* 20, pp. 181–195, 2006.
 47. Smagorinsky, J., “General circulation experiments with the primitive equations,” *Monthly Weather Review* 91(3), 99-164, 1963.
 48. Piomelli, U., Scotti, A., Balaras, E., “Large-Eddy Simulations of Turbulent Flows, from Desktop to Supercomputer,” *Vector and Parallel Processing — VECPAR 2000*, Lecture Notes in Computer Science Volume 1981, 2001, pp 551-577.
 49. Holmes, D. J., “Wind loading of structures,” New York, NY: *Taylor and Francis*; 2007.

50. Chen, F., “HPC user Environment 1”, *HPC user services training courses at Louisiana State University*, spring 2015.
51. Simiu, E., “Design of Buildings for Wind, A Guide for ASCE 7-10 Standard Users and Designers of Special Structures,” *John Wiley & Sons, Inc.*, 2011.
52. Den Hartog, J.P., “Mechanical Vibrations,” *McGraw-Hill Book Company, The Maple Press Company*, York, PA, USA, 1934.
53. Warburton, G.B., and Ayorinde, E.O., “Optimum absorber parameters for simple systems”. *Earthquake Engineering & Structural Dynamics*, 8(3), 197-217, 1980.
54. Simiu, E., and Scanlan, R., “Wind effects on structures,” *John Wiley & Sons*, New York, USA, 1996.
55. Si, Y., Karimi, H.R., Gao, H., “Modelling and optimization of a passive structural control design for a spar-type floating wind turbine,” *Engineering Structures*, 69, 168–182, 2014.
56. Feng, M.Q., and Mita, A. “Vibration control of tall buildings using mega sub-configuration,” *Journal of Engineering Mechanics*, 121 (10), 1082–1088, 1995.